UCL Université catholique de Louvain

École polytechnique de Louvain (EPL)

epl

Large Eddy Simulation of a convective Atmospheric Boundary Layer

Dissertation presented by
Maxime LEJEUNE

for obtaining the Master's degree in
Ingénieur civil mecanicien

supervisorOne(s)
Grégoire WINCKELMANS, Matthieu DUPONCHEEL , Philippe CHATELAIN

Reader
Eric DELEERSNIJDER

Academic year 2017-2018

Acknowledgements

Computational resources have been provided by the supercomputing facilities of the Université catholique de Louvain (CISM/UCL) and the Consortium des Équipements de Calcul Intensif en Fédération Wallonie Bruxelles (CÉCI) funded by the Fond de la Recherche Scientifique de Belgique (F.R.S.-FNRS) under convention 2.5020.11.

Contents

1 Introduction **1**
- 1.1 Scope of this work . . . 2
- 1.2 Outline . . . 3

2 Notions of stability and scaling laws **4**
- 2.1 Notions of thermal atmospheric stability . . . 4
- 2.2 Temporal evolution . . . 5
- 2.3 Scaling laws . . . 6

3 Large Eddy Simulations of the Atmospheric Boundary Layer **9**
- 3.1 Governing equations . . . 10

4 Implementation in BigFlow **12**
- 4.1 BigFlow numerical framework . . . 12
- 4.2 Subgrid scale model . . . 14
  - 4.2.1 Smagorinsky model . . . 14
  - 4.2.2 Scalar SGS diffusivities model . . . 14
  - 4.2.3 Implementation of a scalar SGS model . . . 14
- 4.3 Momentum Wall model . . . 15
  - 4.3.1 Implementation of the wall model . . . 15
  - 4.3.2 Monin-Obukhov similarity theory . . . 17
- 4.4 Scalar flux BC at the wall . . . 18
  - 4.4.1 New scalar flux formulation . . . 18
  - 4.4.2 Reduction of the stencil near the wall . . . 19
  - 4.4.3 Validation: channel flow $Re_\tau = 395$ and $Pr = 0.71$ . . . 21
- 4.5 Upper Boundary condition: sponge layer . . . 25
  - 4.5.1 The different kinds of upper boundary condition . . . 25
  - 4.5.2 Implementation of the sponge layer . . . 26
- 4.6 Description of the overall algorithm . . . 27

5 Application: a dry convective Atmospheric Boundary Layer **30**
- 5.1 Numerical setup . . . 30
- 5.2 Validation of the results and tuning of the coefficients . . . 33
  - 5.2.1 Comparison of the profiles . . . 33
  - 5.2.2 Spectral analysis . . . 38
  - 5.2.3 Impact of the sponge layer parametrization . . . 39
  - 5.2.4 Impact of the SGS Prandtl number . . . 43
- 5.3 Three dimensional structure of the CBL at quasi steady state . . . 43
- 5.4 Conclusion and perspectives . . . 46

6 Conclusion **48**

Bibliography **52**

List of Figures

1.1 Schematic structure of the ABL for aerodynamically rough flow in neutrally stratified conditions . . . 2

2.1 Temporal evolution of the ABL structure on a typical summer day based on Stull [2] 5
2.2 Adimensional Monin-Obukhov vertical velocity profile for different values of the Obukhov length . . . 7

4.1 Sketch of the variable storage system layout . . . 13
4.2 Sketch of a xz cut at of the computational domain in the middle of the cell in direction y for the stress wall model . . . 17
4.3 Steps for the application of the scalar boundary condition . . . 19
4.4 Sketch of a xz cut at of the computational domain in the middle of the cell in direction z for the scalar constant flux boundary condition . . . 21
4.5 Channel flow configuration used by Kawamura . . . 22
4.6 Channel flow at $Re_\tau = 395$ and $Pr = 0.71$: mean temperature profile comparison with Kawamura DNS results . . . 23
4.7 Channel flow at $Re_\tau = 395$ and $Pr = 0.71$: mean RMS temperature profile comparison with Kawamura DNS results . . . 24
4.8 Channel flow at $Re_\tau = 395$ and $Pr = 0.71$: mean turbulent kinematic heat flux profile comparison with Kawamura DNS results . . . 24
4.9 Sketch of a Oxz cut of the computational domain at a bounadry where the sponge layer is applied . . . 27
4.10 Simplified description of the overall algorithm . . . 29

5.1 Scheme of the computational domain and boundary conditions used in the BigFlow implementation . . . 31
5.2 Evolution of the dimensionless height of the inversion base with the dimensionless time for $\mathrm{Pr}_{SGS} = 0.75$ and 0.5 . . . 34
5.3 Mean dimensionless temperature profile $\langle T(z) \rangle$ versus height at $t_* = 6$ . . . 35
5.4 Dimensionless vertical heat flux versus dimensionless height at $t_* = 6.5$ . . . 35
5.5 Dimensionless vertical velocity variance versus dimensionless height at $t_* = 6.5$. 36
5.6 Dimensionless horizontal velocity variance versus dimensionless height at $t_* = 6.5$ 36
5.7 Dimensionless temperature variance versus dimensionless height at $t_* = 6.5$ . . . 37
5.8 Evolution of the mean dimensionless temperature profile $\langle T(z) \rangle$ versus height from $t_* = 2$ to $t_* = 7$ . . . 37
5.9 Normalized horizontal power density spectra of the horizontal velocity component, vertical velocity component, and temperature, versus the dimensionless wave number k/z_i . . . 38
5.10 Evolution of the dimensionless RMS fluctuation profiles of the mean vertical velocity component and potential temperature through the sponge layer for different damping coefficients . . . 40

5.11 Ratio of the power density spectra at the lower edge of the sponge layer z_{SL} and at the upper edge of the domain z_{top} expressed in dB 41
5.12 Normalized horizontal power density spectra of the horizontal velocity component, vertical velocity component, and temperature, versus the dimensionless wave number k/z_i and for various values of the damping constant 42
5.13 Normalized horizontal power density spectra of the horizontal velocity component, vertical velocity component, and temperature, versus the dimensionless wave number k/z_i and for $\mathrm{Pr}_{SGS} = 0.5$ and 0.5 42
5.14 Oxz Cross section of the domain at $t_* = 6$ and averaged from $t_* = 6$ to 7 44
5.15 3D isosurface of the dimensionless temporally averaged temperature over a convective time 44
5.16 Oxy contour plots of the dimensionless vertical velocity and temperature fluctuations field 45
5.17 Simulation of a daily cycle 47

List of Tables

5.1 Comparison of the numerical setups used in this thesis to that of Schmidt & Schumann 32

Chapter 1

Introduction

The Atmospheric Boundary layer (ABL) is the part of the atmosphere in direct contact with the ground we live in. It consequently plays an important role in many fields of our everyday life. The impact of its characteristics ranges from the dispersion of pollutants to the growth of crops. Understanding its governing mechanisms is also crucial in order to develop accurate weather prediction models. Moreover, with the emergence of renewable energies, the ABL topic came at the center of many ongoing researches in the context of wind farms.

A first step toward developing a good comprehension of the ABL and its physics is to introduce a working definition identifying precisely what the term ABL refers to. Such a definition is provided by Garratt [1] who defines the Atmospheric Boundary Layer as:

> *"The layer of air directly above Earth's surface in which the effects of the surface are felt directly on time scales less than a day, and in which significant fluxes of momentum, heat or matter are carried on a scale of the order of the depth of the ABL or less"*

Stull [2] provides a similar definition but considers a different timescale of an hour or less. In essence, the ABL can thus be described as the lower part of the troposphere whose dynamics strongly deviate from the geostrophic balance observed in the free atmosphere as a result of the influence of the planetary surface.

With Reynolds numbers ranging ranging form 10^7 to 10^9 [1][3][4], the ABL is by nature *turbulent*. Its behavior and the characteristics of its turbulent structures are dictated by the complex interactions between various physical phenomenons. The characteristics of the underlying surface impact on the momentum, heat and moisture exchanges while larger scale phenomenons such as the Earth's rotation or subsidence (ie: synoptic scale phenomenons) also impact the overall force balance. A correct parametrization of the *surface fluxes* is essential in order to develop realistic ABL theories. Entire studies are devoted to the topic. The surface fluxes are directly impacted by the topography of the underlying surface. The presence of buildings, hills or even vegetation is among factors that regulate the surface budget thereby making its study extremely complex.

The ABL shares some similarities with the structure of classical boundary layer flows. One can for example distinguish an inner and an outer region in both cases. The *inner surface layer*, consists of the lowest 10% of the ABL. It's also sometimes addressed as the *constant flux layer* because of the assumption of constant fluxes (less than 10% variation) within that layer. This layer in direct contact with the ground is mostly affected by the surface nature. In contrast, the *outer Ekman region*'s physics is mainly dictated by the Coriolis force balance while the dependence on the surface characteristics progressively vanishes as surface gets further away. The lowest part of the inner region is called the *roughness sublayer*. The later is immediately adjacent to the earth surface and is consequently affected by the characteristics of the individual roughness elements. It extends from the surface up to two to five times the height of the

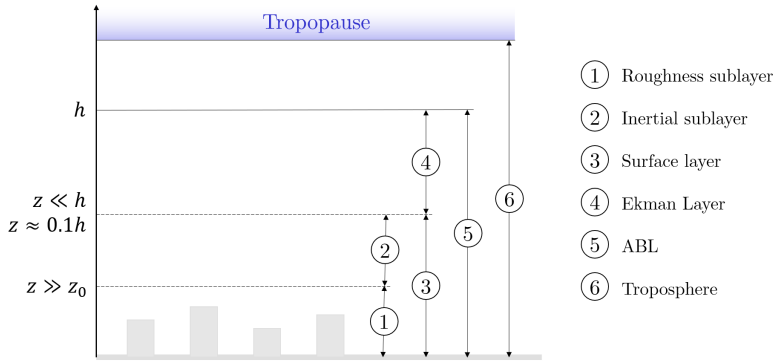

Figure 1.1: Schematic structure of the ABL for aerodynamically rough flow in neutrally stratified conditions based on Garratt [1]

roughness elements, z_0, where the effect of the individual roughness elements disappears and the flow becomes homogeneous. In the context of buoyancy driven convective boundary layers, no distinction is made between the surface layer and the Ekman layer and they are jointly referred to as the *mixing layer*. [1][5][6].

Each of these layers is thus characterized by its own physics. In an attempt to improve our understanding of the ABL, many theories based on campaigns of field measurements and dimensionnal analysis have been introduced since the pioneering work of *Monin and Obukhov* in the mid 1950s [7]. The applicability of these theories however remains rather limited. Moreover they provide a relatively coarse view of the flow and do not allow to effectively capture the small scale motions and fluctuations. The rise of *Computational Fluid Dynamics* (CFD) approaches led to significant improvements of our fundamental understanding of the ABL physics. One of the majors interest of CFD modeling is that it enables to capture motions down to a scale beyond the reach of field data measurements thereby complementing the experimental approaches in an interesting way.

1.1 Scope of this work

The CFD modeling of atmospheric flows is a convoluted process in itself. As mentioned previously ABL flows are inherently linked to turbulence. They are characterized by high Reynolds numbers which make the classical Direct Navier Stockes (DNS) approach unaffordable. The size of the mesh that would be required to capture eddies down to the smallest scale is not achievable given the current computational capabilities. It is precisely in that context that *Large Eddy Simulations* (LES) were initially introduced following the groundbreaking work of Deardorff and Smagorinsky in the early 1950s.

The basic philosophy behind the LES approach is to consider that, beyond a certain scale, motions become more universal and hence easier to model. The energy spectra is then decomposed into two parts: the *resolved term* and the *modeled term*. As indicated by its name, the later, which is also called the Subgrid Scale (SGS) term, is not computed explicitly. It relies on a model to be evaluated. Consequently, a coarser grid can be used while still preserving a sufficient degree of accuracy.

However, some more problems arise from the LES decomposition itself. The two main ones which are dealt with in the context of this thesis are the SGS term and wall parameterizations. Indeed, formulating a SGS scale model that models accurately the SGS physics is still at the center of many ongoing researches. Various models have been formulated but it is still not clear which one should be used. Moreover, as the grids used for LES studies are relatively coarse, the small scales eddies observed in the wall neighborhood are not captured properly resulting in inconsistent behavior of the flow in that region. A possible solution is to use wall models to

correct these discrepancies.

As part of this thesis, a *Convective Boundary Layer* (CBL) was modeled in the LES framework. The simulations were carried using BigFlow , a in-house Navier-Stockes equations numerical solver developed successively by different members of Thermodynamics and Fluid Mechanics team. From the beginning of this work,BigFlow already offered some solid capabilities in the field of LES studies but lacked some essential components to allow an accurate modeling of the scalar fields. The first step of this work thus consisted in implementing a *consistent SGS scalar* model and *realistic boundary conditions*. In term, this allowed us to simulate a CBL and compare the results to actual measurements and CFD data from other authors.

1.2 Outline

Chapter Two first introduces the notions of atmospheric stability. Thermal stability is a topic widely covered in atmospheric sciences which is unseperable from the ABL study. In Chapter Three we explain the basic philosophy of LES simulation and then carry on presenting the Navier-Stockes equations as used in the context of ABL modeling. The next step is to introduce the BigFlow framework and explain how scalar fields modeling is taken care off inBigFlow . This is presented in Chapter Four along with the description of some CBL specific boundary conditions. We end this chapter by providing a simplified description of the overall algorithm used to integrate the velocity and scalar fields in the context of CBL. Finally, in Chapter Six, we apply our finding to a practical test case. Our results are evnentually compared to the ones presented by other authors in order to validate the code. We conclude this last chapter by using our results to develop a first insight of the structure of the CBL.

Chapter 2

Notions of stability and scaling laws

The most common approach is to think of the atmosphere structure in term of *static stability*. Static stability refers to the tendency of the atmosphere to retain its current structure. In other words it characterizes its resistance to upward motions. It can be for example be used to predict the evoluation of the ABL structure through a *standard day cycle*. Static stabilty does however not take the wind shear effect into account while *dynamic stability* does. Some dynamic stability criteria can also be used to formulate *scaling laws* (ie: Monin-Obukhov) that predicts the behavior of the flow in a given layer. These laws are however region depedant: a different scaling applies in the surface layer than in the Ekman layer resulting from the different force balance for example.

In this Chapter we will thus begin by introducing a few notion of static hermal static stability and how they affect the daily evolution of the ABL before moving to the more comprehensive description of the ABL structure provided by dynamic stability considerations along with scaling laws.

2.1 Notions of thermal atmospheric stability

Atmospheric stability studies the atmosphere resistance to upward motions. It is classically associated to the study of the thermodynamics of moist air through the definition of the *virtual potential temperature*. The *virtual temperature* is introduced as:

$$T_v = T\,(1 + 0.61q) \tag{2.1}$$

where T is the absolute temperature of the air and q its specific humidity. The virtual temperature, T_v, is thereby defined as the temperature a theoretical dry air parcel would have the same density as the moist air parcel considered. Following this definition, an expression for the *virtual potential temperature* can be derived from the gas law and the first law of thermodynamics:

$$\theta_v = T_v \left(\frac{p}{p_R}\right)^{-R_d/c_p} \tag{2.2}$$

with R_d the dry air gas constant, c_p its heat capacity and p_R, a reference pressure. The virtual potential temperature is thus the virtual temperature that would result from an air parcel being brought adiabatically from pressure p to the reference pressure.

The use of the *virtual potential temperature* as a state variable considerably simplifies the study of the ABL by removing the temperature variation induced by the pressure changes with altitude. In what will follow we will therefore characterize the ABL state by its potential

virtual tempearture rather than simply by its temperature. Moreover we will only consider dry atmospheric boundary layers, thereby implying $q = 0$. Consequently the virtual potential temperature, θ_v, and the standard potential temperature, θ, will essentially refer to the same concept.

Under the assumption of unsaturated air, one can distinguish three stability regimes based on those definitions. An air parcel is initially at equilibrium at height z and then undergoes a perturbation dz. If the resulting buoyancy forces acts as a restoring force pushing the parcel back to its original height, the atmosphere layer is said to be *statically stable*: $\partial\theta_v/\partial z > 0$. Turbulent Kinetic Energy (TKE) is being destroyed by buoyancy. Conversely, the atmosphere is said to be *statically unstable* when light layers are over topped by denser layers of air, namely colder and/or dryer layers. In that case, the displaced air layer undergoes an even greater destabilizing buoyancy force as it goes up. Equilibrium can therefore not be reached and the parcel is pushed further away from its initial equilibrium position by buoyancy. Unstable atmosphere are associated with $\partial\theta_v/\partial z < 0$ and TKE production. Finally we define the *statically neutral* regime, $\partial\theta_v/\partial z = 0$ in which the perturbed air parcel reaches a new equilibrium at height $z + dz$.

2.2 Temporal evolution

Stability consideration dictates the overall structure of the ABL. The depth and structure of the ABL is however not constant. It varies significantly throughout the days and the seasons depending on various factors such as radiative heating or cooling from the ground, air moisture content, wind magnitude and surface characteristics. The daily evolution of an ABL under standard conditions can be described as follows.

A *diurnal mixing layer* starts developing from the sunrise with the first sun rays heating the soil. The temperature of the air adjacent to the ground consequently starts increasing eventually resulting in the first thermals rising. At this stage, TKE is being produced by buoyancy. The ascension height of those thermals is limited at the top by a strong statically stable air layer, the so called the *inversion layer*. The later initially moves up throughout the day with the progressive penetration of thermal by entrainment until it reaches equilibrium. The resulting unstable mixed layer continues to grow reaching heights of 1 to 2 [km] by the middle of the afternoon.

At sunset, production of TKE by buoyancy ceases, only wind shear TKE production persists. A a result, the diurnal mixing layer collapse. The heat flux at the surface reverse, cooling the nearby air and thereby forming a *stable layer* of air just above the ground. This layer of air slowly expands, gradually destroying the mixed layer formed at daytime. This cooling effect is

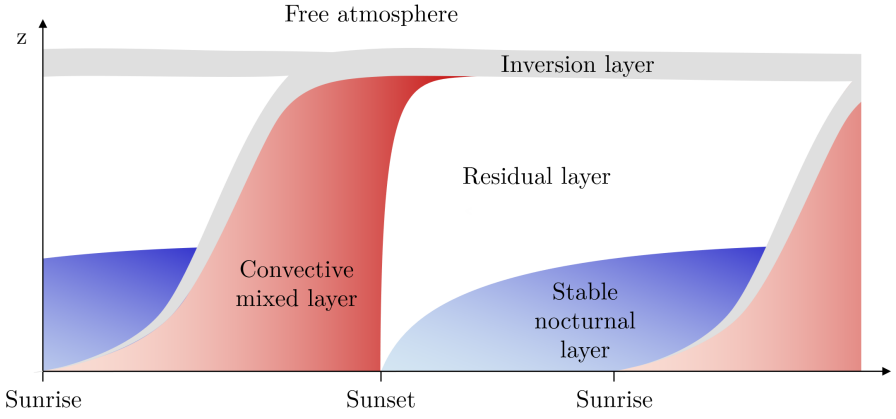

Figure 2.1: Temporal evolution of the ABL structure on a typical summer day based on Stull [2]

however limited and the resulting stable layer thus remains relatively shallow ($\mathcal{O}(10[\text{m}])$). Most of the upper part of the ABL remains unaffected thus keeping the adiabatic lapse rate of the initial mixing layer [2].

2.3 Scaling laws

Static stability criteria only enables to predict the behavior of the flow to a limited extent. In order to predict the mean vertical shape of the scalar and velocity dimensionless profiles, scaling laws have to be introduced. Based on Buckingham Pi theorem, different scaling laws can be defined. This section introduces the different scaling used in the context of this work. *Monin Obukhov similarity theory* for the surface layer is first presented before introducing the associated relevant *scaling for the mixed layer*.

Monin-Obukhov similarity theory: By definition, static stability (*cfr:* : Section 2.1) does not take the effect of wind shear effects into consideration. While TKE can whether be generated or destroyed by buoyancy depending on the stability conditions, wall shear always results in the production of TKE. Therefore various dimensionless dynamic stability parameters accounting for the combined effects of wind shear and buoyancy were introduced in an attempt to remedy to the shortcomings of static theory . One of the most widely used is the so-called *Obukhov stability parameter* which reads:

$$\xi = \frac{z}{L} \tag{2.3}$$

with L, *Obukhov length* defined by:

$$L = -\frac{u_\tau^3 \theta_0}{\kappa g \overline{w'\theta'}} = -\frac{u_\tau^3 \theta_0}{\kappa g q_w} \tag{2.4}$$

θ_0 being the mean flow temperature, κ von Kármán's constant and $q_w = \frac{Q_w}{\rho_0 c_p}$ the kinematic surface heat flux with Q_w the actual surface heat flux. This number has the dimension of a length and may be regarded as a measure of the height above the surface from which buoyancy first dominates shear. The order of magnitude of the Obukhov length typically ranges from one meter to a few tens of meters. Stable stratification ($q_w < 0$) results in a positive length while unstable conditions ($q_w > 0$) translate into negative values. Neutral conditions correspond to $q_w = 0$ and hence $L \to \infty$.

The *Obukhov stability parameter* is particularly useful as it can be used along with dimensional analysis to formulate a modified law of the wall accounting for stratification effects. Monin and Obukhov hypothesized that stratified near wall turbulence could be fully characterized by a set of four dimensional parameters: the friction speed, $u_\tau = \sqrt{\tau_w/\rho}$, the distance from the wall z, the buoyancy parameter, g/θ_v and the wall heat flux $\left(\overline{w'\theta'_v}\right)\big|_w$. Under this assumption, they applied the Buckingham Pi theorem to show that any dimensionless property of the flow could be expressed as an unknown function of the dimensionless parameter ξ. This led them to the formulation of the well-known flux gradient relations. The classical vertical velocity flux gradient relations yields:

$$\frac{\kappa z}{u_\tau}\frac{\partial u}{\partial z} = \phi_m(\xi) \tag{2.5}$$

Similarly, for the temperature gradient relationship:

$$\frac{\kappa z}{\theta_*}\frac{\partial \theta}{\partial z} = \phi_h(\xi) \tag{2.6}$$

where $\theta_* = -\overline{w'\theta'}/u_\tau$. ϕ_m and ϕ_h are referred to as the stability functions and need to be determined empirically [1]. Various parameterizations were introduced throughout the years the most popular being the Businger–Dyer flux-profile relationships [8]:

$$\xi < 0 \ \text{(unstable)}: \qquad \phi_m(\xi) = (1-16\xi)^{-1/4} \qquad \text{and} \qquad \phi_h(\xi) = (1-16\xi)^{-1/2} \tag{2.7}$$

$$\xi > 0 \ \text{(stable)}: \qquad \phi_m(\xi) = 1+5\xi \qquad \text{and} \qquad \phi_h(\xi) = 1+5\xi \tag{2.8}$$

In this theory, the dimensionless velocity and temperature profiles are obtained by integration of the previous relations from height z_0 to an arbitrary height z. This yields:

$$\frac{u(z)}{u_\tau} = \frac{1}{\kappa}\left[\ln\left(\frac{z}{z_0}\right) - \Psi_m\left(\frac{z}{L}\right) + \Psi_m\left(\frac{z_0}{L}\right)\right] \tag{2.9}$$

$$\frac{\theta(z)-\theta_w}{\theta_*} = \frac{1}{\kappa}\left[\ln\left(\frac{z}{z_0}\right) - \Psi_h\left(\frac{z}{L}\right) + \Psi_h\left(\frac{z_0}{L}\right)\right] \tag{2.10}$$

where Ψ_m and Ψ_h are the so called correction functions. They can be expressed as:

$$\Psi_{m/h}(\xi) = \int_0^\xi \frac{1-\phi_{m/h}(\xi(z))}{z}\mathrm{d}z \tag{2.11}$$

Integration of the previous equation in the stable case leads to:

$$\Psi_m(\xi) = 2\ln\left(\frac{1+\phi_m^{-1}}{2}\right) + \ln\left(\frac{1+\phi_m^{-2}}{2}\right) - 2\arctan\left(\phi_m^{-1}\right) + \frac{\pi}{2} \tag{2.12}$$

$$\Psi_h(\xi) = 2\ln\left(\frac{1+\phi_h^{-1}}{2}\right) \tag{2.13}$$

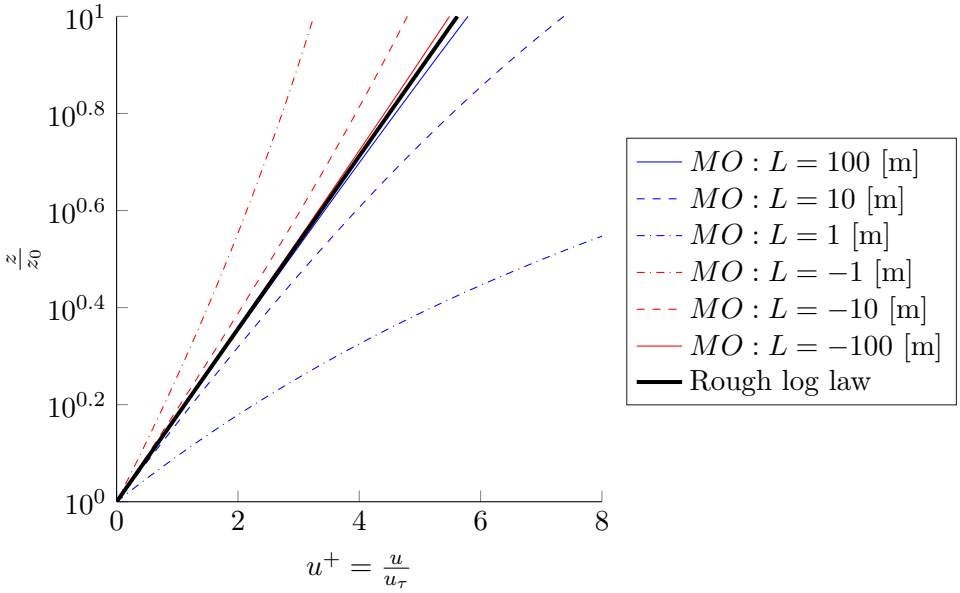

Figure 2.2: Adimensional Monin-Obukhov vertical velocity profile for different values of the Obukhov length - red: unstable case (ie: $L < 0$) and blue: stable case (ie: $L > 0$) - black thick line corresponds to neutral case (ie: $L \to \infty$) which is equivalent to the standard rough log law

while in the stable case, it becomes:

$$\Psi_m = -5\xi \tag{2.14}$$

$$\Psi_h = -5\xi \tag{2.15}$$

Fig. 2.2 provides a comparison of typical horizontal velocity profiles computed from Eq. 2.9. We can effectively check that the Monin-Obukhov profile tends toward that of the rough law of wall as the wall heat flux decreases and thus as the Obukhov length tends toward infinity.

Convective mixed layer scaling : Monin Obukhov scaling is however only applicable in the surface layer. Above the surface layer in the mixed layer, (ie: $0.1z_i < z < 0.9z_i$) a different scaling takes application. Far away from the surface, the flow becomes insensitive to the surface bellow and is primarily driven the the buoyant turbulent motions. As shown by Deardoorff the relevant scales to nondimensionalize the the statical properties of turbulence in that layer are respectively w_C^n, the velocity convective scales and w_C^n, temperature convective scale [8]:

$$w_C^n = \left(\frac{g q_w z_i^n}{\theta_0}\right)^{1/3}, \qquad \theta_C^n = \frac{q_w}{z_i^n}, \qquad t_C^n = \frac{z_i^0}{w_C^n} \tag{2.16}$$

The n superscripts refers to the dimensionless time, t_*, considered.The resulting dimensionless statistics can then be expressed as functions of z/z_i only with, z_i, the height of the inversion layer. The later is defined as the height at which the vertical heat flux, $\langle w'\theta' \rangle$, reaches its minimum [9]. Similarly to Monin-Obukhov theory in the mixed layer, the relevant convective scaling can be used to derive an expression of the dimensionlesss profiles inside the mixed layer, this will however not be presented here.

Chapter 3

Large Eddy Simulations of the Atmospheric Boundary Layer

As already mentioned previously, the study of ABL is inherently linked to that of turbulent motions. Typical velocity ABL ranges from 1 [ms^{-1}] at the bottom of the domain to 10 [ms^{-1}] at the top. The associated characteristic horizontal length scale is about 10 [km] in both horizontal direction while the ABL extends up to heights of the order of 1[km]. [4]. The Reynolds numbers (ranging from $\mathcal{O}(10^7)$ to $\mathcal{O}(10^9)$) encountered in ABL flows are consequently too high too allow DNS simulations. Garratt [1] suggests that the number of grid points required to resolve explicitly the smallest eddies scales like:

$$N_x\, N_y\, N_z \propto Re^{9/4} \tag{3.1}$$

Such a grid is obviously unaffordable in this context. This appears even more evident as we further factor in the cost of the temporal integration associated with the use of such a fine mesh. In an attempt to fix these limitations, new methods were developed: one of them being the Large Eddy Simulation (LES) approach.

The development of the LES methods finds its roots in the attempts of Deardorff and Smagorinsky [10] to develop new CFD techniques that could be applied to atmospheric flows. The basic idea behind LES is to decompose the energy spectra into a resolved and a unresolved part, the so called subgrid scale (SGS). This decomposition relies on the hypothesis that largest eddies contain most of the energy and are the ones responsible of most of the transport processes. The small scales eddies on the other hand are assumed to be more universal and hence easier to model. As a result, only the largest eddies are explicitly resolved while the SGS eddies are modeled. Since the smallest scales no longer need to be explicity solved, a coarser mesh can be used thereby remedying to the shortcomings of DNS approach. The decomposition of a generic field, ϕ, into an unresolved, ϕ', and a resolved part, $\bar{\phi}$, reads:

$$\phi = \bar{\phi} + \phi' \tag{3.2}$$

The resulting Navier-Stockes equations in the context of ABL along with the main underlying hypothesis are introduced in the next Section.

3.1 Governing equations

Under Boussinesq assumption, the filtered continuity, momentum and scalar conservation equations in their incompressible form read [11]:

$$\frac{\partial \bar{u}_j}{\partial x_j} = 0 \tag{3.3}$$

$$\frac{\partial \bar{u}_i}{\partial t} + \bar{u}_j \frac{\partial \bar{u}_i}{\partial x_j} = -\frac{\partial \bar{p}}{\partial x_i} + g\frac{\bar{\theta} - \theta_0}{\theta_0} + \nu \frac{\partial^2 \bar{u}_i}{\partial x_j \partial x_j} - \frac{\partial \tau_{ij}^{SGS}}{\partial x_j}\delta_{i3} + \mathcal{S}_{\mathbf{u}i} \tag{3.4}$$

$$\frac{\partial \bar{\theta}}{\partial t} + \bar{u}_j \frac{\partial \bar{\theta}}{\partial x_j} = \alpha \frac{\partial^2 \bar{\theta}}{\partial x_j \partial x_j} - \frac{\partial q_{\theta j}^{SGS}}{\partial x_j} + \mathcal{S}_\theta \tag{3.5}$$

with summation indice over j. $\bar{u}_i$ are the filtered components of the three dimensional velocity field and $\bar{\theta}$ is the potential temperature scalar field. Generally speaking, Eq. (3.5) remains however applicable to any scalar field. In what will follow, the notation $(\cdot)_1$, $(\cdot)_2$, $(\cdot)_3$ and $(\cdot)_x$, $(\cdot)_y$, $(\cdot)_z$ are used interchangeably and the filtering operator $\overline{(\cdot)}$ is often out for concisness.

The LES filtering operation introduces two additional terms accounting for the phenomenons not captured by the grid. We will refer to them as the *subgrid scale (SGS) terms*. The anisotropic part of the SGS stress tensor τ_{ij}^R reads $\tau_{ij}^{SGS} = \tau_{ij}^R - \frac{2}{3}k_s\delta_{ij}$, with $k_s = \frac{1}{2}\tau_{ii}^R$ being the SGS kinetic energy. Based on Boussinesq's turbulent-viscosity hypothesis, it can be related to the filtered strain rate tensor, $\bar{\mathcal{S}}_{ij}$ [3]:

$$\tau_{ij}^R = \overline{u_i u_j} - \bar{u}_i \bar{u}_j \tag{3.6}$$

$$\tau_{ij}^{SGS} \overset{\text{m}}{=} -\nu_{SGS}\left(\frac{\partial \bar{u}_i}{\partial x_j} - \frac{\partial \bar{u}_j}{\partial x_i}\right) = -2\,\nu_{SGS}\,\bar{\mathcal{S}}_{ij} \tag{3.7}$$

Similarly,

$$q_{\theta j}^{SGS} = \overline{u_j \theta} - \bar{u}_i \bar{\theta} \overset{\text{m}}{=} -\alpha_{SGS}\,\frac{\partial \bar{\theta}_i}{\partial x_j} \tag{3.8}$$

ν_{SGS} and α_{SGS} respectively denote the *subgrig scale (SGS) viscosity* and *subgrid scale scalar diffusivity*. Various models are available: which of them should be used is a complex question and is still an ongoing research topic. The SGS term modelization used in this work is presented in more details in Section 4.2.

Following the definition of the anisotropic SGS stress tensor τ_{ij}^R, we introduce the *filtered modified pressure* defined as $\bar{P} = \frac{\bar{p}}{\rho_0} + \frac{2}{3}k_s - p_\infty$, where p_∞ is the mean background pressure.

The right-hand side of Eq. (3.4) features two more terms. The first one (second from the left) is the *Boussinesq buoyancy* term. It is derived under the assumption that the variation of density are only in the buoyancy term, $(\rho - \rho_0)g$. Introducing the coefficient of thermal expansion yields, $\beta = 1/\theta_0$:

$$\begin{aligned}\Delta\rho g = (\rho - \rho_0)g &= -\rho_0\beta(\theta - \theta_0) \\ &= -\rho_0 g\frac{\theta - \theta_0}{\theta_0}\end{aligned} \tag{3.9}$$

This term allows natural convection by coupling the velocity field to the temperature field. The term $\mathcal{S}_{\mathbf{u}i}$ includes the contributions of the different kinds of forcing possible. This forcing term

can be chosen in order to enforce a Coriolis forcing or to mimic the force exerted on the flow by a wind turbine (ie: actuator surface/line model). It can also represent the forcing term used by some type of absorbing boundary condition. More information about this application are provided in Section 4.5).

The scalar conservation equation, Eq. (3.5), can be applied to any scalar field. The standard scalar fields studied in the context of ABL are the humidity and temperature fields (potential temperature if we deal with moist air). Many studies also deal with the transport of pollutants or particles inside the ABL. Implementing a moist ABL model was beyond the scope of this work because it requires a strong coupling between the different fields due to the more complex moist air thermodynamics. We thus chose to limit ourself to a simple temperature field which already provided us with enough modelization challenges. However the boundary conditions developed should in principle remain valid for any other scalar field.

We already introduced, $q_{\theta j}^{SGS}$, the scalar SGS flux previously, the only term left is thus $\mathcal{S}_\theta$. In the code developed, the sole purpose of this term is once again to be able to enforce some specific types of boundary conditions. Generally speaking it can also be used to model the phase changes, radiation heating and so on but for the sake of simplicity these applications were not considered here.

Finally, we will note that most authors (eg: [11], [12], [13]) tend to leave out the molecular viscosities and diffusivities, arguing that their order of magnitude in below the ones of the SGS terms in the context of ABL. This assumption seems fair given we are dealing high Reynolds number flows.

Chapter 4

Implementation in BigFlow

BigFlow is a in-house Navier-Stockes equations numerical solver developed successively by different members of Thermodynamics and Fluid Mechanics team. It was initially developed by Georges [14] and Bricteux [15] as part of their PhD thesis. The code was then completely rewritten by Duponcheel [16], in order to improve its modularity and its efficiency (improvements of the Poisson solver). Further work was finally provided by Thiry [17] in order to implement wall sheer stress models for LES of wall bounded flows.

BigFlow thus already offered some solid flow modeling capabilities in the framework of the LES study of wall bounded flows. However the implementation of some new features was further required in order to accurately model scalar fields in LES studies. To begin with, a *SGS model for scalar* had to be implemented. Following which, a *constant scalar flux* boundary condition accounting for the variable scalar SGS diffusivity was developed. Moreover, some *ABL specific boundary conditions* also had to be enforced (ie: use of Monin Obukhov similarity theory and of an upper Rayleigh-Friction damping layer). All of those aspects are more largely discussed in the next few sections. As a conclusion, the overall structure of the solver and the interaction between its different parts is presented.

4.1 BigFlow numerical framework

The BigFlow code is an incompressible Navier-Stockes equations numerical solver. It uses fourth order finite difference schemes on stretched Cartesian grids based on the schemes developed by Vasilyev [18]. The boundary conditions are thus enforced using up to three layers of ghost points. The variables are stored on a staggered structured Cartesian mesh following Harlow and Welsh's [19] Marker and Cell (MAC) arrangement. The MAC storage arrangement used is illustrated on Fig. 4.1. For what will follow, the reader should take note that the scalar flux, $\mathcal{Q}_{\theta i}$, is stored at the same location as the u_i velocity component while the SGS diffusivities, α_{SGS}, are provided at the center of the cell.

In order to make the next sections more understandable, we will now introduce a few notations to properly write the schemes. The mesh can be stretched using a one dimensional mapping:

$$\frac{x_i}{L_i} = f(\xi_i) \tag{4.1}$$

$x_i \in [0; L_i]$ being the physical coordinate and $\xi \in [0; 1]$ its computational equivalent. This stretching can be particularly useful in order to run wall resolved flow simulations at a reasonable computational cost.

The differentiation operator in direction ξ_1 applied to an arbitrary field ϕ with a stencil of width $n\Delta_1$ (Δ_1 being the uniform grid spacing in the computational domain in the direction ξ_1)

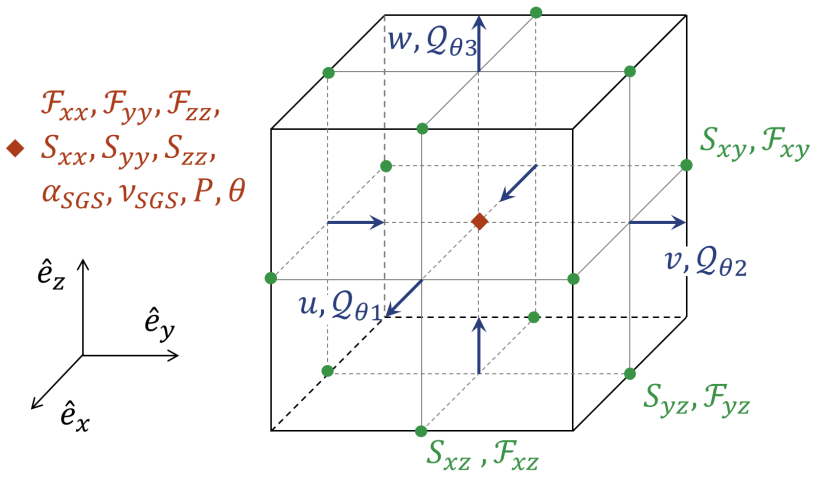

Figure 4.1: Sketch of the variable storage system layout

is given by:

$$\frac{\delta_n \phi}{\delta_n \xi_1} \triangleq = \frac{\phi(\xi_1 + \frac{n}{2}\Delta_1,\ \xi_2,\ \xi_3) - \phi(\xi_1 - \frac{n}{2}\Delta_1,\ \xi_2,\ \xi_3)}{n\Delta_1} \tag{4.2}$$

Following this definition, the Jacobians of the mapping (Eq. (4.1)) in the direction ξ_i is denoted:

$$J_{i,n} \triangleq \frac{\delta_n x_i}{\delta_n \xi_i} \tag{4.3}$$

without summation over the direction index, i. This finally allows us to define the fourth order differentiation operator in direction ξ_i:

$$\frac{\partial \phi}{\partial x_i} \simeq \{\mathcal{D}_i^n(\phi)\}_n^{1,3} \triangleq \frac{9}{8}\mathcal{D}_i^1(\phi) - \frac{1}{8}\mathcal{D}_i^3(\phi) \tag{4.4}$$

where $\mathcal{D}$ is the generic differentiation operator defined as:

$$\mathcal{D}_i^n = \frac{1}{J_{i,n}} \frac{\delta_n \phi}{\delta_n \xi_i} \tag{4.5}$$

The fourth order differentiation operator is thus essentially a linear combination of two first order differentiation operators of respective width Δ_1 and $3\Delta_1$.

To end with, it is often necessary to interpolate the fields. Using the notation we just presented, the interpolation operator in the direction ξ_1 reads:

$$\bar{\phi}^{n,\xi_1} \triangleq \frac{1}{2}\left(\phi(\xi_1 + \frac{n}{2}\Delta_1,\ \xi_2,\ \xi_3) + \phi(\xi_1 - \frac{n}{2}\Delta_1,\ \xi_2,\ \xi_3)\right) \tag{4.6}$$

The unsteady Navier-Stockes equations are solved using a fractionnal step method which consists in a reprojection of a predictor velocity field, obtained by a classical time integration, onto a divergence free space. As this work mostly focuses on the integration of the scalar conservation equation, we will not provide more explanations about the pressure reprojection method. More details on the topic can be found in Duponcheel [16].

4.2 Subgrid scale model

As already mentioned in Section 3.1, the modelization of the SGS term is a complex research topic in itself. Many SGS models, most of which relying on the concept of SGS vsicosity, were developped throughout the years since the groundbreaking work of Smagorinsky [10] and Lilly [20] in the mid 1960s. The choice of the SGS parametization is crucial since the correct turbulent dissipation characteristics relies on the good characteristics of the SGS model.

4.2.1 Smagorinsky model

Smagorsinsky [10] proposed a simple relation linking the magnitude of the resolved strain rate tensor, $|\bar{S}|$, to the SGS viscosity, ν_{SGS}, by analogy with *Prandtl's mixing length hypothesis*:

$$\nu_{SGS} = \ell_s^2 \, |\bar{S}| = (C_S \Delta)^2 \, |\bar{S}| \tag{4.7}$$

where:

$$|\bar{S}| = \left(2\bar{S}_{ij}\bar{S}_{ij}\right)^{1/2} \tag{4.8}$$

and ℓ_S is a length scale equivalent to the mixing-length scale and $\Delta = (\Delta_x \Delta_y \Delta_z)^{1/3}$ is the equivalent grid size. C_S is the *Smagorinsky coefficient*, to be specified. Under the assumptions of homogeneous and isotropic turbulence at high Reynolds number, Lilly [20] determined that the theoretical value of C_S is roughly 0.17 if the resolved scales are located in the inertial subrange. In practice, many authors found C_S to be flow and numerics dependent and preferred values ranging from 0.1 to 0.65 [21] [22].

Despite its apparent simplicity, this parametrization performs quite well and is still widely used nowadays (eg: [11], [21]). For the sake of simplicity, we will also use this model for our simulations, with $C_S = 0.17$. We should however acknowledge its limitations, its major limitation being that it is found to be over dissipative in the near wall region. Indeed, in this region the length scale, ℓ_S defined is no longer relevant. As we use wall model LES, this is not a limitation in our work.

4.2.2 Scalar SGS diffusivities model

At this point, the *SGS scalar diffusivities*, α_{SGS}, are still to be parametrized. A common approach is to assume that the SGS Prandtl number, Pr_{SGS}, is constant, and hence take:

$$\alpha_{SGS} = \frac{\nu_{SGS}}{\mathrm{Pr}_{SGS}} \tag{4.9}$$

A similar definition can be used for the Schmidt number. The problem is thus once again to determine which value should be used for Pr_{SGS}. In the context of ABL, different values, $[...0,4...0,7...]$ can be found in the literature [11] [23], [24] [25] [26]. The impact of this coefficient for the study of the ABL is studied in more details in Section 5.2.4.

4.2.3 Implementation of a scalar SGS model

From the beginning of this work, the BigFlow code was able to compute the SGS term for the integration of momentum but it lacked a way to take the SGS term into account for scalars. Computing the SGS diffusivities was straightforward as it only required to implement Eq. (4.9) into the existing framework.

Computing the diffusive term, $\boldsymbol{\mathcal{Q}}_D = (\alpha + \alpha_{SGS})\nabla\,\theta$, was slightly more complicated since the existing code was only able to deal with constant diffusivities, while the α_{SGS} of course varies across the domain (as does ν_{SGS}). We do have that:

$$\nabla \cdot \boldsymbol{\mathcal{Q}}_D = \nabla \cdot [(\alpha + \alpha_{SGS})\nabla\,\theta] \tag{4.10}$$

As hinted previously, the SGS diffusivities therefore need to be interpolated at the center of the cell's faces (rather than at the pressure points: *cfr:* Fig. 4.1) in order to be able a apply a consistent centered difference scheme. Once the interpolated diffusivities are computed, determining the diffusive term is done using Eq. (4.4):

$$\mathcal{Q}_{D,i} \quad \simeq \quad \left(\alpha + \left\{\overline{\alpha}_{SGS}^{n,\xi_i}\right\}_n^{1,3}\right)\left\{\mathcal{D}_i^n(\theta)\right\}_n^{1,3} \tag{4.11}$$

and

$$\frac{\partial \mathcal{Q}_{D,i}}{\partial x_i} \quad \simeq \quad \left\{\mathcal{D}_i^n(\mathcal{Q}_D)\right\}_n^{1,3} \tag{4.12}$$

In practice, in the initial version of the code, the divergence was computed straightaway, without using any intermediate $\boldsymbol{\mathcal{Q}}_D$ field. That was initially done using a constant differentiation stencil, applied directly to the the scalar field θ. Such a stencil could not be used here since α_{SGS} was not considered previously. A new local variable stencil accounting for the variable SGS diffusivity was thus implemented.

The results were validated against classical channel flow benchmark cases. Their validation is presented in Section 4.4.1 along with that of a new modified scalar differentiation scheme.

4.3 Momentum Wall model

Close to the wall, the size of the energy-carrying eddies shrinks and scales with the to distance to the wall [27]. For high Reynolds number flows, such as the ones encountered in the ABL context, using a grid fine enough to effectively capture the near-wall motions comes at a prohibitive computational cost and is therefore not achievable. Both the DNS and wall resolved LES approaches fail in that respect [17]. The solution is thus to use wall modeled LES. In this section we explain how wall models are dealt with in the BigFlow framework and then apply the Monin Obukhov similarity theory to the computation of the wall shear stress.

4.3.1 Implementation of the wall model

As part of his PhD thesis, Thiry [17] implemented a wall shear stress boundary condition that allows to perform wall resolved LES. This boundary condition reads:

$$\boldsymbol{\mathcal{F}}\Big|_\Gamma \cdot \mathbf{n} \;=\; \tau_w \tag{4.13}$$

$$\mathbf{u}\Big|_\Gamma \cdot \mathbf{n} \;=\; 0 \tag{4.14}$$

with $\boldsymbol{\mathcal{F}}$, the momentum flux tensor defined as: $\mathcal{F}_{ij} = -u_i u_j + P\delta_{ij} + 2(\nu + \nu_{SGS})S_{ij}$ where $P = p/\rho$ is the reduced pressure. In order to be able to impose this set of boundary conditions, he developed and validated a new *flux conserving* version of the code. In this form, the time derivative of the velocity is given as the divergence of this momentum flux tensor. The continuity and momentum conservation equations are rewritten as:

$$\frac{\partial u_j}{\partial x_j} = 0 \tag{4.15}$$

$$\frac{\partial u_i}{\partial t} = \frac{\partial \mathcal{F}_{ij}}{\partial x_j} \tag{4.16}$$

As illustrated on Fig. 4.1, the $\boldsymbol{\mathcal{F}}$ component corresponding the wall shear stress is stored exactly at the wall which is convenient as it allows to directly enforce the desired value of the wall shear stress according to Eq. (4.13).

The main problem he was then left with is that the stencil for the computation of the diffusive and convective terms can involve up to three layers of ghost points beyond the wall Γ. Most of the time, standard boundary conditions (ie: Dirichlet, Neumann or symmetry) are used to update the values of these ghost points at each time step, enforcing the boundary condition in the process. However, the wall shear stress boundary condition, Eq. (4.13), is not applied through the use of ghost points. The information contained in the ghost points for the wall parallel velocity components is thus not relevant and cannot be used for the computation of the derivatives. Consequently, the wall normal derivatives are reverted to order 2 in the wall neighborhood.

This *transition from order 4 to order 2* is not harmless. It implies a correction term to be added in the transition zone in order to keep the flux conserving properties of the scheme. Introducing the following 1D generic equation in infinite domain

$$\frac{\partial u}{\partial t} = \frac{\partial \phi(u)}{\partial z} \tag{4.17}$$

Thiry showed that, given a 1D mesh of uniform spacing h and on a staggered grid, the momentum budget resulting from this transition at height z_I was:

$$\frac{d}{dt}\int u\, dz \simeq -\frac{1}{12}\left(\phi_I - \frac{1}{2}(\phi_{I+1} + \phi_{I-1})\right) \tag{4.18}$$

which can also be rewritten as a Taylor series around $z_{I-1/2}$:

$$-\frac{1}{12}\left(\phi_I - \frac{1}{2}(\phi_{I+1} + \phi_{I-1})\right) = \frac{1}{24}\,h^2\,\frac{\partial^2 \phi}{\partial z^2}(z_{I-1/2}) + \mathcal{O}(h^3) \tag{4.19}$$

The transition from the fourth order to the second order thus introduces an error in momentum budget of order 2 at the last point when the second order derivatives are evaluated at $(z_{I-1/2})$.

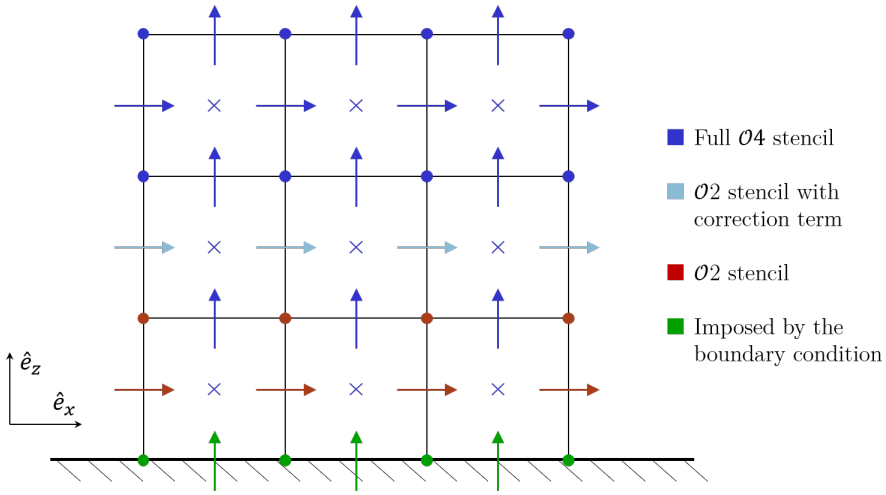

Figure 4.2: Sketch of a xz cut at of the computational domain in the middle of the cell in direction y for the shear stress wall model - arrows: u and w velocities / circles points: $\mathcal{F}_{xz}$ / cross points $\mathcal{F}_{xx}$ and $\mathcal{F}_{zz}$. Based on Thiry [17]

Thiry suggested to introduce a correction term in order to adjust the momentum budget:

$$\left(\frac{\partial \phi}{\partial z}\right)^h (z_{I-1/2}) = \frac{(\phi_I - \phi_{I-1})}{h} + \frac{1}{12}\left(\phi_I - \frac{1}{2}(\phi_{I+1} + \phi_{I-1})\right) \tag{4.20}$$

The resulting scheme conserves momentum in a discrete sense but is only first order accurate on the layer of points concerned by the transition of order $(z_{I-1/2})$. The overall scheme is best summed up by 4.2.

A final issue is that the value of the SGS term initially computed in the first cell is inaccurate. This problem arises once again because of the coarse nature of the grid. Thiry thus implemented a correction of the value of the SGS viscosity. For more details about this aspect or about the overall implementation and the derivation of the wall model, the reader is referred to Thiry [17].

4.3.2 Monin-Obukhov similarity theory

Eq. (4.13) however relies on a model to evaluate the wall shear stress. Various approach can be considered, the one used here is similar to that of Schumann [28]. It assumes the wall shear stress to be aligned with the local velocity vector:

$$\tau_{wi} = -\rho_0 u_\tau^2 \frac{u_i}{|\hat{\mathbf{u}}|_H} \qquad \text{for } i = 1, 2 \tag{4.21}$$

where u_i is the instantaneous i velocity component at the first grid cell adjacent to the wall ($\Delta_z/2$ for a wall with an outward z normal) and $|\hat{\mathbf{u}}|_H = (\hat{u}^2 + \hat{v}_2^2)^{1/2}$ is the local averaged horizontal velocity magnitude. The hat operator denotes a local horizontal average. Assuming that the first grid points lies within the surface layer, the friction velocity, u_τ, can be determined using Monin-Obukhov similarity theory (*cfr:* Section 2.3) thereby introducing the stability parameter $\xi = z/L$ Recalling equations 2.9, the friction speed can be computed as:

$$u_\tau = \frac{|\hat{\mathbf{u}}(z)|_H}{u^+_{MO}(z)} = \frac{\kappa|\hat{\mathbf{u}}(z)|_H}{\ln\left(\frac{z}{z_0}\right) - \Psi_m\left(\frac{z}{L}\right) + \Psi_m\left(\frac{z_0}{L}\right)} \tag{4.22}$$

where u^+_{MO} is theoretical Monin-Obukhov non-dimensional velocity profile. The resulting expression is evaluated at the first cell (ie: $z = \Delta_z/2$) along with Eq. (4.21) to approximate the wall shear stress. One should however note that the resulting set of equations is implicit, as computing u_τ requires to know the Obukhov length $L(u_\tau)$ *a priori*. It can nonetheless be relatively easily be implemented in the existing framework.

4.4 Scalar flux BC at the wall

A key characteristic of the ABL according to the definition introduced by Garratt [1] is that the ABL is the layer of air in which "*significant fluxes of momentum, heat or matter are carried on a scale of the order of the depth of the ABL or less*". Therefore, the correct parametrization of these fluxes is essential in order to develop accurate ABL models.

Many ABL simulation setups prescribe fixed scalar fluxes in the bottom of the domain. These flux conditions are used to model the heat, moisture or matter exchanges between the ground and the ABL. Implementing this kind of boundary condition in the context of DNS simulation is straightforward and is classically enforced through a Neumann boundary conditions. However due to the coarse nature of the meshes used for ABL modeling, the wall scalar flux reads:

$$q_{w,z} = -(\alpha + \alpha_{SGS})\,\frac{\partial\theta}{\partial z} \tag{4.23}$$

Defining a consistent Neumann boundary condition requires to determine the exact value of α_{SGS} at the wall. Moreover, using a scalar model along with a momentum wall model such as the one implemented in the BigFlow framework (Section 4.3) would lead to erroneous results. Indeed the computation of the scalar convective term relies on having access to the value of the velocity field in the ghost points which is not possible considering the implementation of the wall model. A workaround is to enforce an extension of the boundary condition introduced by Thiry [17] to scalars.

4.4.1 New scalar flux formulation

In this section the new wall scalar flux boundary condition is applied to the temperature scalar field. The reasoning can nonetheless be effortlessly extended to any other scalar field. The code developed should therefore remain valid regardless of the scalar field considered.

In order to allow an easy implementation of the scalar flux boundary condition, a new discretization of the scalar conservation equation was introduced. In the initial version of the code which we will refer to as the `DIVSEP` version, the scalar conservation equation reads:

$$\begin{aligned}\frac{\partial\theta}{\partial t} &= \nabla\cdot\Big((\alpha + \alpha_{SGS})\,\nabla\theta\Big)\nabla\cdot\Big(\theta\mathbf{u}\Big)\\ &= \nabla\cdot\boldsymbol{\mathcal{Q}}_D + \nabla\cdot\boldsymbol{\mathcal{Q}}_C\end{aligned} \tag{4.24}$$

The main problem encountered with this initial implementation arises from the fact the divergence of the diffusive term, $\nabla\cdot\boldsymbol{\mathcal{Q}}_D$, is computed straightaway, without using any intermediate field.

Yet, the final goal is the impose a boundary condition such that:

$$\boldsymbol{\mathcal{Q}}\Big|_{\Gamma} \cdot \mathbf{n} \;=\; q_w \tag{4.25}$$

where q_w, the *kinematic heat flux*, is directly related to, Q_w, the sensible heat flux:

$$q_w \;=\; \frac{Q_w}{\rho c_p} \tag{4.26}$$

Applying Eq. (4.25) requires to have access to the scalar kinematic heat flux $\boldsymbol{\mathcal{Q}}|_{\Gamma}$ at the surface, which was not possible in the initial implementation. Therefore a new version of the code in which the time derivative of the temperature field θ is given as the divergence of the kinematic heat flux vector, $\boldsymbol{\mathcal{Q}}$, was developed:

$$\begin{aligned}\frac{\partial \theta}{\partial t} &= \nabla \cdot \Big(\left(\alpha + \alpha_{SGS}\right) \nabla\theta - \theta \mathbf{u} \Big) \\ &= \nabla \cdot \Big(\boldsymbol{\mathcal{Q}}_D + \boldsymbol{\mathcal{Q}}_C \Big) \\ &= \nabla \cdot \Big(\boldsymbol{\mathcal{Q}} \Big)\end{aligned} \tag{4.27}$$

This scheme was named `DIVQ` . It was tested against the scheme `DIVSEP` and yielded the exact same results. In other words, the differentiation stencil is identical but is applied in a different ways. In the `DIVQ` version, the kinematic heat flux vector is computed first and then the divergence operator is applied, allowing to enforce the boundary condition in between these two steps. This is best illustrated by Fig. 4.3. Once again, the MAC mesh layout (Fig. 4.1) is convenient as the wall normal heat flux is provided exactly at the wall. Enforcing the wall heat flux is thus straightforward.

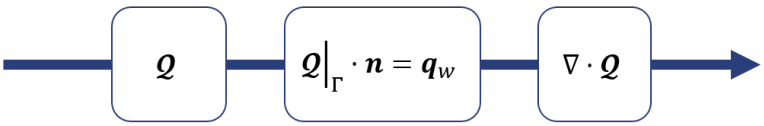

Figure 4.3: Steps for the application of the scalar boundary condition

4.4.2 Reduction of the stencil near the wall

Recalling the notations introduced in Section 4.1, the scheme used in `DIVQ` to compute the $\mathcal{Q}_i$ term can be translated as follows:

$$\mathcal{Q}_i \;\simeq\; \left(\alpha + \left\{\overline{\alpha}^{n,\xi_i}_{SGS}\right\}_n^{1,3}\right) \left\{\mathcal{D}_i^n(\theta)\right\}_n^{1,3} \;+\; \left\{\overline{\theta}^{n,\xi_i}\right\}_n^{1,3} u_i \tag{4.28}$$

The divergence of the temperature is evaluated on a three cells wide stencil while the temperature and SGS diffusivities need to be interpolated at the center of the face whose normal corresponds to the one of the outward kinematic heat flux (ie: same location as the velocity component in the same direction). Given the size of the stencil, we are thus facing the same problem as previously for the wall shear stress model: in this wall scalar boundary condition formulation, the information fetched into the cells beyond the solid wall Γ is inconsistent and cannot be used. The stencil consequently needs to be adapted in the near wall region for the wall normal component of the kinematic heat flux.

Let's consider, without loss of generality, a heat flux on wall whose normal is oriented along the z direction. The stencil for the wall normal kinematic heat flux, $\mathcal{Q}_3$, has to be reverted to order 2 in the wall proximity. The scheme becomes:

$$\mathcal{Q}_3 \quad \simeq \quad \left(\alpha + \overline{\alpha}^{1,\xi_3}_{SGS}\right) \mathcal{D}^1_3(\theta) \quad - \quad \overline{\theta}^{1,\xi_3}\, w \tag{4.29}$$

Only the wall normal component needs to be adapted indeed the wall parallel kinematic heat flux does not require any information from beyond the wall in order to be computed using the full stencil. The value of $\mathcal{Q}_i$ on the first layer of point (ie: the wall) is simply deduced from the boundary condition. Then the kinematic heat flux on the second layer of point is evaluated using this second order reduced stencil while it transition back to the full stencil from the third layer of points above the surface.

The way $\nabla \cdot \boldsymbol{\mathcal{Q}}$ is computed also needs to be changed. The full fourth order stencil simply reads:

$$\frac{\partial \mathcal{Q}_i}{\partial x_i} \simeq \{\mathcal{D}^n_i(\mathcal{Q}_i)\}^{1,3}_n \tag{4.30}$$

with a summation over the i index. The temperature at the center of the first cell is then computed using a degraded version of this scheme for the wall normal direction only, the resulting scheme can be written as:

$$\frac{\partial \mathcal{Q}_i}{\partial x_i} \simeq \{\mathcal{D}^n_1(\mathcal{Q}_1)\}^{1,3}_n + \{\mathcal{D}^n_2(\mathcal{Q}_2)\}^{1,3}_n + \mathcal{D}^1_3(\mathcal{Q}_3) \tag{4.31}$$

However the transition from order 2 to order 4 comes at the price of a of an error in the conservation of the enthalpy budget (ie: $\frac{d}{dt}\int \rho c_p \theta \mathrm{d}z$). Indeed, the same reasoning as for the error in momentum (Section 4.3) can be applied. Introducing the generic 1D model equation in infinite domain:

$$\frac{\partial \theta}{\partial t} = \frac{\partial \phi(\theta)}{\partial z} \tag{4.32}$$

On a 1D uniform staggered grid of spacing h, the budget for the transition of order 2 to order 4 resulting from a transition at height $z_{I+1/2}$ reads:

$$\frac{d}{dt}\int \theta \; dz \simeq -\frac{1}{12}\left(\phi_{I+1/2} - \frac{1}{2}(\phi_{I+3/2} + \phi_{I-1/2})\right) \tag{4.33}$$

This is exactly the same expression as previously, it was simply offset by $h/2$ away from the wall. For more information about the complete derivation of the following set of equations, the reader is thus referred to Thiry [17]. Similarly to was was done for the velocity field, the enthalpy budget is corrected by subtracting the error term while evaluating the derivative at the transition

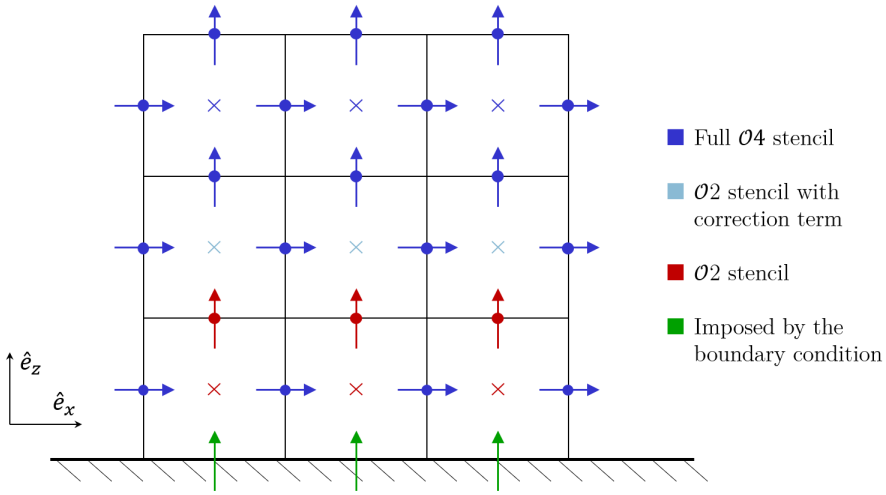

Figure 4.4: Sketch of a xz cut at of the computational domain in the middle of the cell in direction z for the scalar constant flux boundary condition - arrows u and v velocities and $\mathcal{Q}_1$ and $\mathcal{Q}_2$ components of the kinematic heat flux / circles points: interpolated value of α_{SGS} and θ / cross points: θ temperature field.

point (z_I):

$$\left(\frac{\mathrm{d}\phi}{\mathrm{d}z}\right)^h(z_I) \simeq \frac{\phi_{I+1/2} - \phi_{I+3/2}}{h} + \frac{1}{12}\left(\phi_{I-1/2} - \frac{1}{2}(\phi_{I+3/2} + \phi_{I-1/2})\right) \tag{4.34}$$

$$\simeq \frac{\mathrm{d}\phi}{\mathrm{d}z}(z_I) - h\frac{1}{24}\frac{\mathrm{d}^2\phi}{\mathrm{d}z^2}(z_I) + \mathcal{O}(h^2) \tag{4.35}$$

where the last equation can be obtained expressing Eq. (4.33) as a Taylor series expansion around z. Correcting the enthalpy balance consequently results in the the transition layer being only first order accurate. As illustrated on Fig. 4.4, the first layer of points (z_{I-1}) is computed using the second order stencil. The order 2 stencil is also applied to the second layer (z_I) along with the correction term while the scheme transitions back to the full stencil from the third layer of point and on.

4.4.3 Validation: channel flow $Re_\tau = 395$ and $Pr = 0.71$

The code developed is validated against a benchmark DNS solution of heat transfer in turbulent channel flows. Our results are compared to the reference solution obtained by Kawamura [29] for $Re_\tau = 395$ and $Pr = 0.71$ with, Re_τ, the Reynolds friction number defined as:

$$Re_\tau = \frac{u_\tau h}{\nu} \tag{4.36}$$

The setup consists of a fully turbulent channel flow with uniform heating, $\bar{Q}_w$ from both walls. Both walls are parallel to the O_{xz} plane. Hence, the flow only varies in the wall normal direction (x) while it is homogenous in the streamwise (y) and spanwise (z) directions. The computational domain is a periodic box of size $L_x \times L_y \times L_z = 2\pi h \times 2h \times \pi h$ where h is the half channel width.

The flow is driven by a constant forcing pressure gradient. The value of the driving pressure

gradient is selected to ensure conservation of momentum. Recalling the definition of Re_τ, it reads:

$$\left(\frac{\mathrm{d}P}{\mathrm{d}x}\right)_F = -\frac{u_\tau^2}{h}$$

Both plates are heated by a uniform heat flux, $\bar{Q}_w$:

$$\bar{Q}_w = \rho\, c_p\, h\, \langle \bar{u} \rangle \frac{\mathrm{d}\theta_w}{\mathrm{d}x} \tag{4.37}$$

$\langle \bar{u} \rangle$ being the time and space averaged streamwise velocity. Leaving out the SGS term for conciseness, the energy conservation equation, Eq. (3.5), reads:

$$\frac{\partial \theta}{\partial t} + \bar{u}_j \frac{\partial \theta}{\partial x_j} = \frac{\partial}{\partial x_j}\left((\alpha + \alpha_{SGS})\, \frac{\partial \theta}{\partial x_j} \right) \tag{4.38}$$

In this case, because of the wall heat flux, the statistically averaged temperature will increase linearly along the channel which is not compatible with the symmetry assumption. We thus introduce θ_m, the modified temperature:

$$\theta_m = \frac{\mathrm{d}\theta_w}{\mathrm{d}x} x - \theta \tag{4.39}$$

The energy conservation equation for θ_m can then be rewritten as:

$$\frac{\partial \theta_m}{\partial t} + u_j \frac{\partial \theta_m}{\partial x_j} = \frac{\partial}{\partial x_j}\left((\alpha + \alpha_{SGS})\, \frac{\partial \theta}{\partial x_j} \right) + u \frac{\mathrm{d}\theta_w}{\mathrm{d}x} \tag{4.40}$$

where the second term of the right hand-side allows the use of periodic boundary conditions by compensating for the temperature increase along the channel. Dirichlet boundary conditions can then be enforced along both plates while a symmetry condition is used on the remaining surfaces.

Numerically, the grid is the same as the one used by Bricteux and al. [30]. The grid is $N_x \times N_y \times N_z = 64 \times 48 \times 48$. In order to ensure the first grid point lies within the viscous sublayer, a stretching is used in the wall normal direction, x:

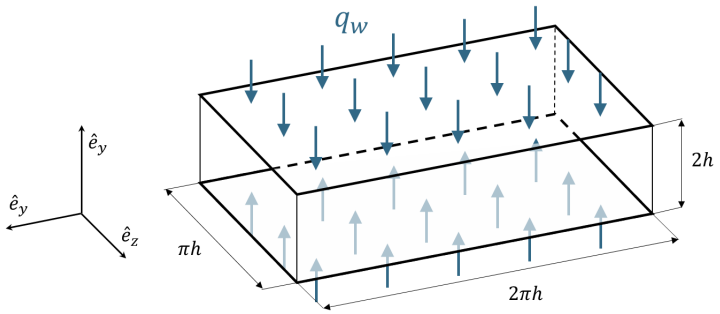

Figure 4.5: Channel flow configuration used by Kawamura [29]

$$\frac{y}{h} = 1 + \frac{\tanh(\gamma(\xi - 1))}{\tanh(\gamma)} \tag{4.41}$$

where $y \in [0 : 2h]$ is the x coordinate of the grid point considered and $\xi \in [0 : 2]$ its numerical equivalent. $\gamma = 2.75$ is chosen so that the viscous sublayer is captured. The simulation is thus wall-resolved and does not require any momentum and heat flux wall model to be used.

The version of the code used is the flux preserving version developed by Thiry [17] since we will use it extensively later to model the ABL. Following Thiry, a WALE SGS model is used for the SGS momentum term with $C_{WALE} = 0.15$. We further assume that $\mathrm{Pr}_{SGS} = 0.85$ to remain constant.

The code is run with a converged channel flow solution as initial condition and the results are averaged over 5 convective times. Three different test cases are considered in order to asses the performances of the various versions of the code and of the boundary conditions developed:

- **Dirichlet**: $\theta_m(\pm h) = 0$, same boundary condition as the one used by Kawamura, used to validate the new `DIVQ` scheme and LES term implementation.
- **Constant scalar flux**: $\boldsymbol{\mathcal{Q}}|_\Gamma \cdot \mathbf{n} = q_w$ the uniform scalar flux buncary condition developed in the context of this work.
- **Neumann**: $\alpha \frac{\partial \theta_m}{\partial y}(\pm h) = q_w$ which should be equivalent to the flux condition developed as the LES is here wall resolved.

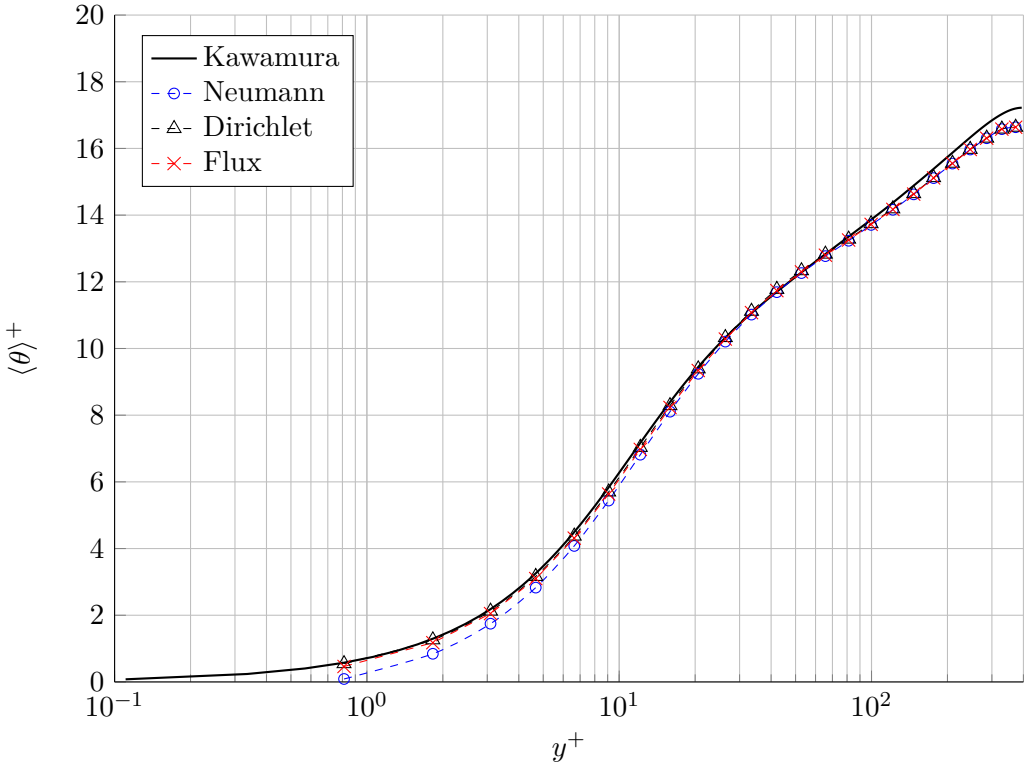

Figure 4.6: Channel flow at $Re_\tau = 395$ and $Pr = 0.71$: mean temperature profile comparison with Kawamura DNS results - Thick black line: Kawamura reference data - Blue circle: Neumann BBoundary condition - Black triangle: Dirichlet Boundary condition - Red cross: New Flux Boundary condition

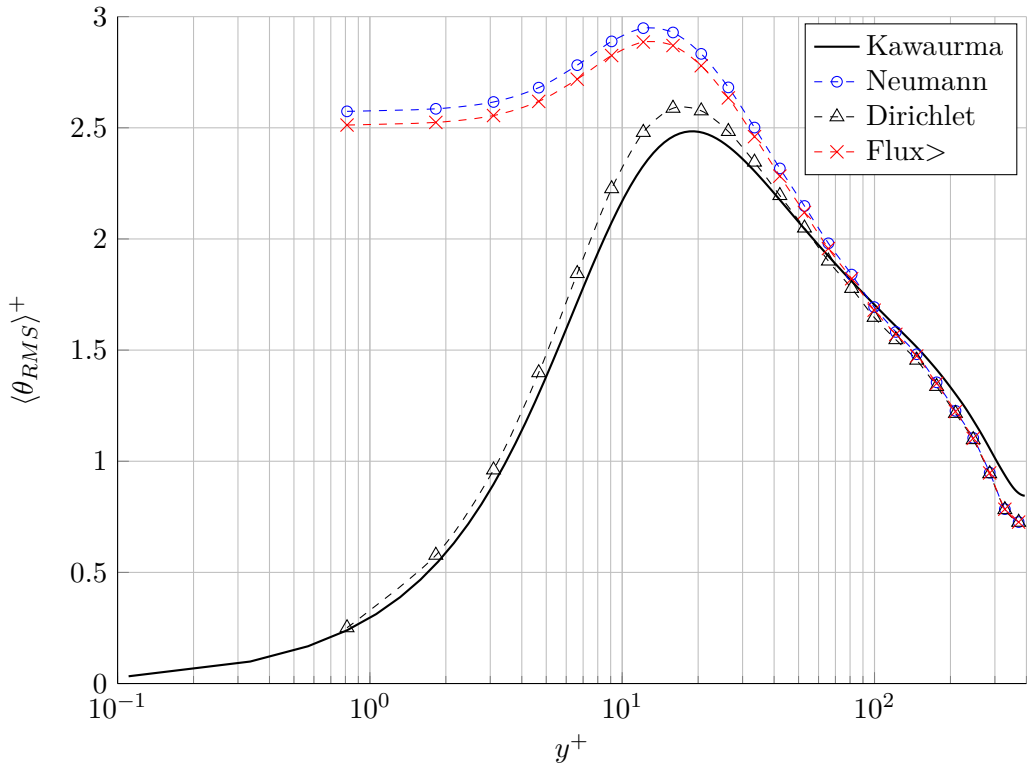

Figure 4.7: Channel flow at $Re_\tau = 395$ and $Pr = 0.71$: mean RMS temperature profile comparison with Kawamura DNS results - Thick black line: Kawamura reference data - Blue circle: Neumann BBoundary condition - Black triangle: Dirichlet Boundary condition - Red cross: New Flux Boundary condition

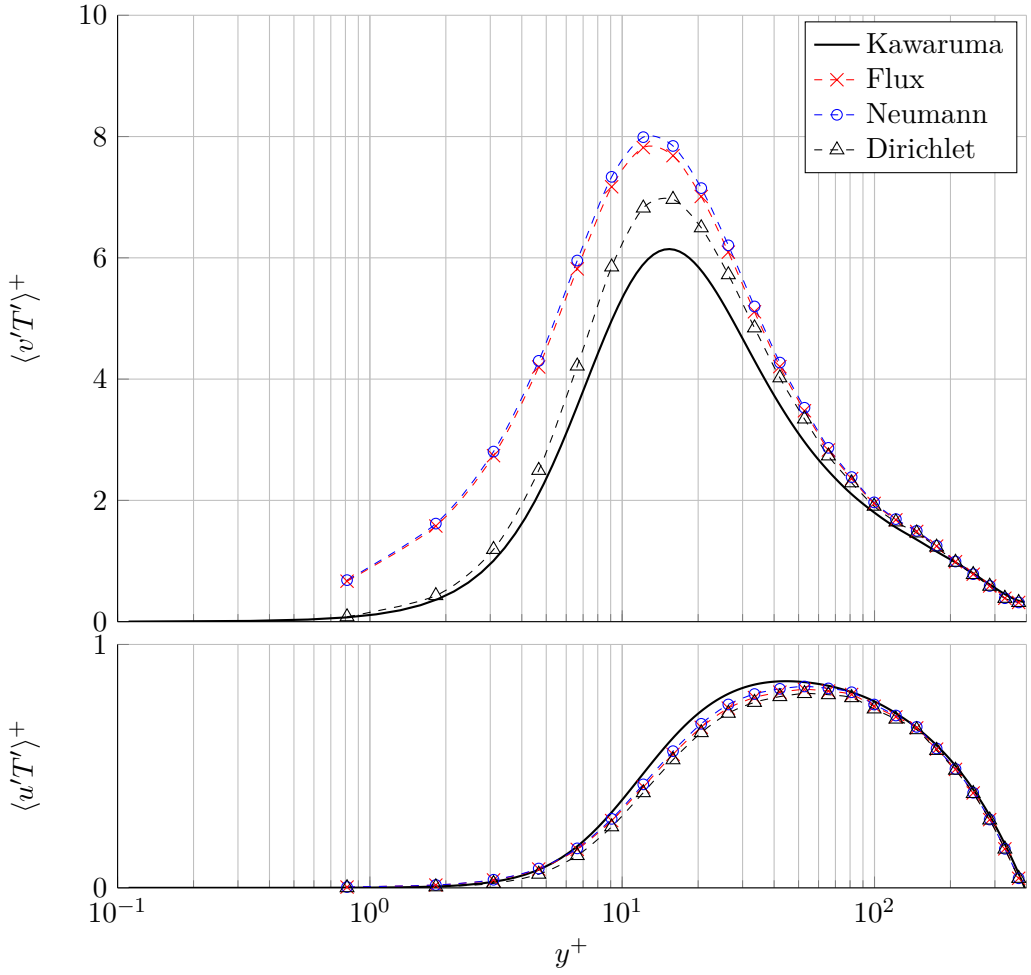

Figure 4.8: Channel flow at $Re_\tau = 395$ and $Pr = 0.71$: mean turbulent kinematic heat flux profile comparison with Kawamura DNS results - Thick black line: Kawamura reference data - Blue circle: Neumann BBoundary condition - Black triangle: Dirichlet Boundary condition - Red cross: New Flux Boundary condition

The corresponding averaged temperature and fluctuation profiles are depicted on Figs. 4.6 to 4.8. The friction velocity u_τ and friction temperature $\theta_\tau = q_w/u_\tau$ are used as representative scales for the adimensionalization.

The first step is to evaluate whether or not the `DIVQ` version of the code achieves sufficient accuracy. Therefore, the `DIVQ` version of the code is used to simulate a heated channel flow with temperature enforced at both walls, thus Dirichlet. The results are plotted and compared to the Kawamura benchmark solution. Overall, they lead to similar results. The averaged temperature profile shows strong agreeement with Kawamura data except toward the center of the channel where a slight deviation can be observed. The $\langle\theta_{RMS}\rangle^+$, $\langle v'T'\rangle^+$ and $\langle w'\theta'\rangle^+$ profiles also match the reference profiles pretty well, though some of the values suffer a small offset. However these small offsets are unavoidable since the LES integration of the velocity field in itself is already responsible for part of those inaccuracies (*cfr:* Thiry [17]). Overall the new scheme thus appears to provide satisfactory results thereby validating the new `DIVQ` scheme.

The new flux boundary condition must in turn be tested and validated using a similar setup. In order to ensure a fair comparison, the results are compared to that resulting from the use of a standard Neumann boundary condition (which was already validated in the past) which does not rely on the reduced stencil in the near wall region. Once again the results are in agreement with Kawamura DNS data for the mean dimensionless temperature profile. The same cannot be said from the averaged fluctuation profiles in the near wall area. The RMS temperature fluctuations profile remains roughly constant through the viscous sublayer. The fact both the Neumann and the new flux condition lead to the same result however validate the implementation. The difference in the RMS temperature profile hence directly results from the nature of the boundary condition used. Previous studies dealing with the impact of the choice of the boundary condition on the turbulent statistics led to similar results (eg: [31]).

4.5 Upper Boundary condition: sponge layer

The numerical simulation domain used to model the ABL is inevitably finite. All models consequently require an upper boundary condition to be specified at the top of the simulation domain. This boundary condition lacks physical ground. It should therefore mimic the behaviour of the surrounding fluid as closely as possible. This notably implies that disturbances such as gravity waves should be able to leave the domain without generating spurious reflections. In this section, we describe different approaches to deal with the upper boundary condition and then introduce the boundary condition that was implemented in BigFlow as part of this work.

4.5.1 The different kinds of upper boundary condition

One can distinguish three main types of boundary conditions: the rigid lid, the radiation boundary condition and, finally, the absorbing layer (also referred to as the sponge layer). Assessing how each of them impacts the solution and understanding their mathematical formulation is the first step toward implementing one of them in the BigFlow framework.

The *rigid lid boundary condition* is essentially a solid wall condition ($w|_\Gamma = 0$ with w the boundary normal component of the velocity vector). Consequently it results in total reflection of the incoming gravity waves which can disrupt the solution. It is however trivial to implement.

The second type of boundary condition is the *radiation boundary condition*. A commonly used radiation condition formulation is the one derived by Klemp and Durran ([32]) from linear internal wave theory. Under the Boussinesq assumption and the hypothesis of 2D linear hydrostatic flow

with no Coriolis effects, they obtained a local boundary condition:

$$\hat{p}(z,t) = \frac{\rho_0 N}{k}\hat{w}(z,t) \tag{4.42}$$

where N is the Brunt–Väisälä frequency and $\hat{p}$ and $\hat{w}$, the Fourier coefficients of p and w respectively. Both $\hat{p}$ and $\hat{w}$ are expressed in terms of the horizontal wave number, k, making this condition hard to implement. Moreover, more advanced theories have to be introduced in order to deal with more complex flows since the hypothesis underlying this formulation are quite restrictive. Its main advantage lays in the fact that only a minor increase in computational cost is required to apply it.

A conceptually simpler, yet effective type of boundary condition is the *sponge layers*. This boundary condition adds an absorbing layer on top of the physical domain. The disturbances are freely allowed inside that zone but are damped out once in. Various type of sponge layer can be considered with the two most common ones being the *Rayleigh friction* (the variables are relaxed toward a reference state) and the *diffusive damping* (artificial increase of the eddy diffusivity in the sponge layer). Their conceptual simplicity and ease of implementation comes at the price of a significant increase in computational cost due to the extended size of the computational domain. Sponge layers are also subject to reflection. Tuning their coefficients is tricky as excessive values of those coefficients would lead to more reflection while insufficient values would not allow sufficient damping making the sponge layer useless [33].

4.5.2 Implementation of the sponge layer

A *Rayleigh friction* layer spanning height z_{SL} to z_{top} is introduced in the uppermost part of the domain. This choice was primarily dictated by the ease of implementation of this kind of boundary condition combined to its extensive use in literature. This absorbing boundary layer however does not alleviate the need for a proper boundary condition to be formulated at the top of the domain (z_{top}) where a rigid lid boundary condition is consequently enforced. The resulting computational setup is illustrated on Fig. 4.9.

For a model variable ϕ, a generic formulation of the Rayleigh friction relaxation term reads:

$$\mathcal{S}_{\phi,SL} = \gamma(z)\,\Big(\phi(\mathbf{x}) - \bar{\phi}(z)\Big) \tag{4.43}$$

where $\gamma(z)$ is an height dependent coefficient and z is the wall normal direction. In this configuration, the flow is relaxed toward a prognostic solution $\bar{\phi}$ with a time scale $\gamma^{-1}(z)$ [s^{-1}] which depends on the distance from the upper boundary. Abrupt changes in $\gamma(z)$ may induce reflexion. Therefore $\gamma(z)$ was chosen as a smoothly increasing function of z [33]:

$$\gamma(z) = \gamma_d\,\sin^2\left(\frac{z - z_{SL}}{z_{top} - z_{SL}}\right) \tag{4.44}$$

Providing a universal optimal value for γ_d is impossible as its tuning is case dependent. The value used throughout this thesis was somehow arbitrarily set to 0.005. A more comprehensive study of the impact of this coefficient is presented in Section 5.2.3.

The depth of the absorbing layer $d_{SL} = z_{top} - z_{SL}$ also impacts the behaviour of the sponge layer. A significant part of the domain has to be dedicated to the sponge layer in order to ensure

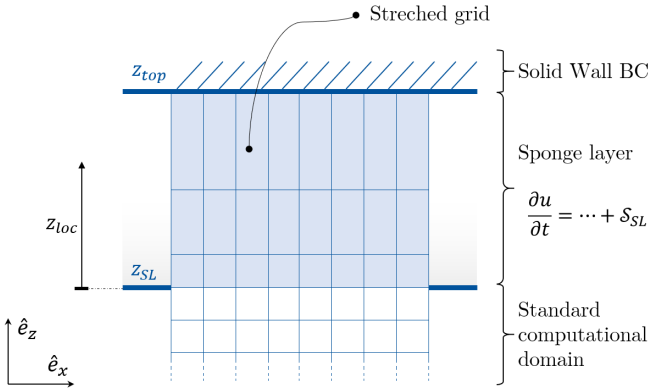

Figure 4.9: Sketch of a Oxz cut of the computational domain at a bounadry where the sponge layer is applied

its good performances. Most authors use a sponge layers whose depth ranges from 20 to 30% of the total height of the physical domain (eg: [34], [35] and [36]). As mentioned previously, this extended vertical size is associated with a higher computational cost which can nonetheless be reduced using a grid stretching in the upper part of the domain.

The implementation of the sponge layer in BigFlow is pretty straightforward as it does not require the computation of any additional term besides the height dependent coefficient $\gamma(z)$ and of the reference profile $\bar{\phi}$. Both uniform and linear profiles can be used for the reference profile. A sponge local coordinate system, z_{loc}, is also introduced to make the computation more readily understandable. It simply reads:

$$z_{loc} = |z - z_{SL}| \tag{4.45}$$

This local coordinate system makes it easier to generalize the implementation of this boundary condition to any wall of the domain.

4.6 Description of the overall algorithm

This section aims at providing a more global view of the code. A simplified overall description of the Navier-Stockes solver implemented in `navierStockes.c` is depicted by Fig. 4.10. The reader should however note that it was voluntarily kept relatively basic to keep the focus on the specific parts of the code used and/or implemented in the context of this work. Some elements such as the complete time stepping scheme were willingly left out. Moreover the integration scheme presented here is only strictly valid for the integration of the velocity and temperature fields (Eqs. (3.3)-(3.5)) in the context of ABL. It can nonetheless be extended to more general cases with little effort.

The code can be divided in two main parts: the velocity and scalar temporal integrators. Even though each of them uses a different time stepping scheme, their overall algorithm remains mostly the same.

The first step is to compute the SGS viscosities, ν_{SGS}, and thermal diffusivities, α_{SGS}. The velocity integration is carried first, which is convenient as the SGS viscosity field is required in order to compute the scalar diffusivity fields. Evaluating the SGS viscosity is done using a Smagorinsky model. The viscosities are then corrected in the near wall region. Following which, the diffusivities can be calculated assuming a constant SGS Prandtl number, Pr_{SGS} (*cfr:* Section 4.2).

The momentum flux tensor, $\mathcal{F}_{ij}$, and scalar flux vector, $\mathcal{Q}_i$, are then evaluated. This is

achieved using the expression developed in Sections 4.3 and 4.4 which were adapted in the wall neighborhood area to avoid using any irrelevant data contained in the ghost points beyond the solid walls. The velocity field is fed to the scalar integrator in order to compute the convective part of the scalar flux tensor at time t^n. The wall model is then applied to both the velocity and the scalar temperature field. A uniform flux scalar wall model is used for the temperature field while the computation of the wall shear stress is based on Monin-Obukhov similarity theory.

The right handside (RHS) of Navier-Stockes equations can finally be determined adding up the divergence of the fields to contributions of the various source terms. The divergence stencil is also adapted in the cells close to the wall and the momentum/enthalpy correction terms are applied. As to the source terms, they represent different contributions. The source term associated to the velocity field are the buoyancy term denoted $B(T)$ and the source term corresponding to the sponge layer $\boldsymbol{\mathcal{S}}_{\mathbf{u},SL}$ (*cfr:* Section 4.5). $B(T)$ requires the temperature field at time t^n to be calculated. The temperature field on the other hand is only associated to the sponge layer source term $\mathcal{S}_{T,SL}$.

Once the RHS is computed for all the fields, the standard boundary conditions (ie: Neumann, Dirichlet or symmetry) are enforced and the time stepping is performed. The velocity field further goes through a pressure reprojection step to correct the initial guess computed.

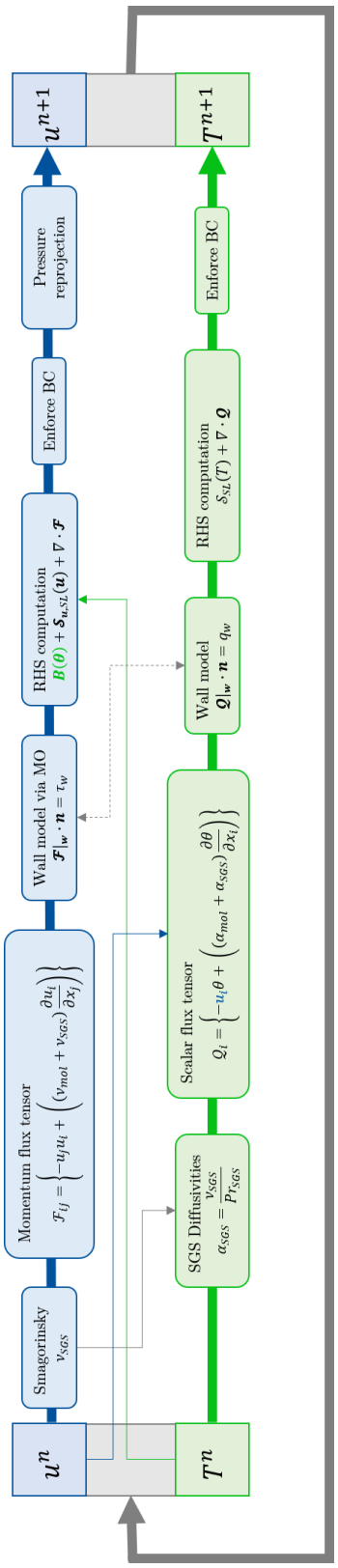

Figure 4.10: Simplified description of the overall algorithm

Chapter 5

Application: a dry convective Atmospheric Boundary Layer

As mentioned previously, on a typical *sunny day and under weak wind conditions*, a sharp super adiabatic layer forms on top of the ground due to the radiative heating provided by the surface. As a result of the degraded stability conditions, buoyant plumes start to ascend progressively merging together, thereby forming larger *buoyant structures*. Initially their ascend is limited to the bottom of the domain but as time passes they gradually extend to higher altitude ultimately reach the inversion base. The resulting layer is addressed as the *mixed layer*.

Owing to their relative conceptual simplicity Convective Boundary Layers (CBLs) have been at the center of many studies since the pioneering work of Deardorff in 1970 [37]. Nowadays the mechanism regulating CBL are relatively well understood and consequently provide us with a framework for the validation of atmopsheric LES codes. In their article "*Coherent structure of the convective boundary layer derived from large eddy simulation*" [9] published in 1989, Schmidt & Schumann investigated the structure of a convective uniformly heated boundary layer with zero mean wind using LES. To this day this article stands as a reference and similar setups are still widely used. For example, as part of his thesis in 2013, Dall'Ozzo validated his code against Schmidt & Schumann and obtained similar results [21].

The first part of this section introduces the computational setup used for the simulations. Focus is laid on the main differences between our setup and that of Schmidt & Schumann . We then move on to validating the code against the results of Schmidt & Schumann , essentially based on mean profiles considerations and study the influence of different parameters of our model on the results. Finally, we use those results to analyze the three dimensional coherent structures encountered in the CBL and compare them to what is described in the literature.

5.1 Numerical setup

In this Section, we first present the numerical setup used by Schmidt & Schumann [9] before highlighting its main differences compared to the one used in the context of this work

Schmidt & Schumann numerical setup: The case investigated corresponds to a Convective Boundary Layer (CBL) uniformly heated from below and topped by a layer of uniformly stratified fluid (ie: the inversion layer). The mean horizontal wind is zero, meaning the TKE production is dominated by the buoyancy term. The conservation equations are identical to the ones introduced in Section 3.1. However, in Schmidt & Schumann model, the SGS model is based on a TKE prognostic equation rather than on Smagorinsky theory.

The numerical values are typical of to the ones encountered on a sunny day in southern Germany. The fluid studied is dry air whose molecular kinematic viscosity and diffusivty are respectively: $\nu = 15 \times 10^{-6}$ [ms^{-1}] and $\alpha = 21.4 \times 10^{-6}$ [ms^{-1}]. The ground is heated by an

uniform kinematic heat flux, $q_w = 0.06$ [Kms^{-1}]. Monin–Obukhov similarity theory with a roughness height $z_0 = 0.16$ [m] is applied to determine the wall shear stress at the interface between the air and the ground. Schmidt & Schumann also introduce a radiation boundary condition [32] at the top of the domain to avoid spurious reflections of gravity waves. A Neumann type boundary condition corresponding to the strength of the inversion layer is further enforced at the top of the domain: $\partial\theta/\partial z = 0.003$ [Km^{-1}]. As to the lateral boundary conditions, periodicity is assumed.

Numerically the system used by Schmidt & Schumann is a periodic box of size $N_x \times N_y \times N_z = 160 \times 160 \times 48$ for a physical domain of size $L_x \times L_y \times L_z = 8000\,[\mathrm{m}] \times 8000\,[\mathrm{m}] \times 2400\,[\mathrm{m}]$. The spacial resolution is thus uniform in all three directions $\Delta_x = \Delta_y = \Delta_z = 50$ [m].

The initial height of the inversion layer is also used to specify the initial condition. The initial temperature profile corresponds to the that of a mixed layer initially at $\theta_0 = 299.715$ [K] topped by an inversion layer of uniform stability $\mathrm{d}\langle\theta\rangle/\mathrm{d}z = 0.003$ [Km^{-1}]. Both temperature and velocity profiles are disturbed by a variable perturbation r randomly selected in $[-0.5;\ 0.5]$. The initial temperature profiles thus reads:

$$\theta(z) = \begin{cases} \theta_0 + 0.1\, r \left(1 - \frac{z}{z_m}\right) \theta_C^0, & \text{if } 0 < z \leq z_{z_m} \\ \theta_0 + (z - z_m) \frac{\mathrm{d}\langle\theta\rangle}{\mathrm{d}z}, & \text{if } z > z_m \end{cases} \tag{5.1}$$

similarly, the initial velocity profile is given by:

$$w(z) = \begin{cases} 0.1\, r \left(1 - \frac{z}{z_m}\right) w_C^0, & \text{if } 0 < z \leq z_m \\ 0, & \text{if } z > z_m \end{cases} \tag{5.2}$$

where $z_m = 1350$ [m] is the initial height of the mixed layer. These initial conditions are engineered so that they lead to the inversion laying at height $z_i^{ref} = 1600$ [m] at $t_* = 6$. They result in the following values of the convective scales: (*cfr:* : 2.3):

$$w_C^0 = 1.46\ [\mathrm{ms}^{-1}] \qquad \text{and} \qquad \theta_C^0 = 0.041\ [\mathrm{K}] \tag{5.3}$$

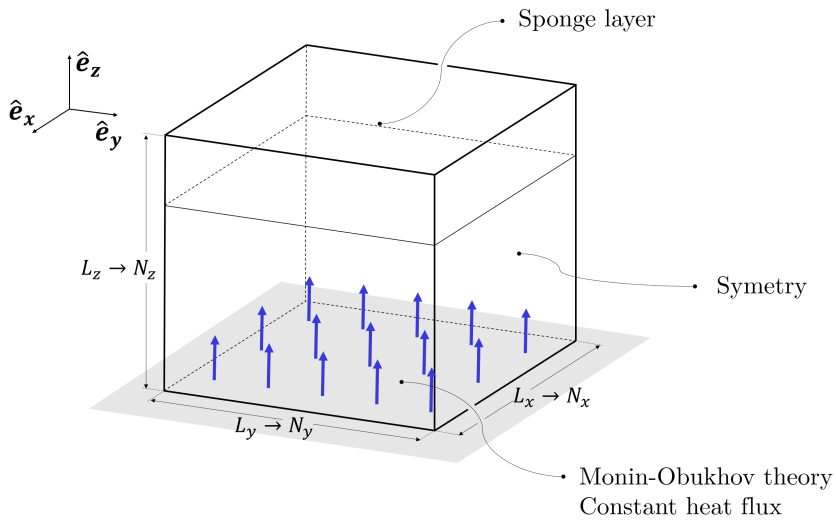

Figure 5.1: Scheme of the computational domain and boundary conditions used in the BigFlow implementation

Modifications to the setup: The simulation setup used in the context of this work slightly differs from the one of Schmidt & Schumann. As indicated previously, the SGS model used relies on Smagorinsky theory rather than on a prognostic equation for the TKE. The boundary conditions are overall the same except the upper velocity boundary condition where a sponge absorbing layer ($\gamma_d = 0.05$ [s^{-1}]) is applied instead of a radiation condition. The velocity profile is relaxed toward a zero velocity state while the reference temperature profile corresponds to that of the inversion layer:

$$\boldsymbol{\mathcal{S}}_{\mathbf{u},SL} = \gamma(z)\,\Big[\mathbf{u}(\mathbf{x}) - \mathbf{0.0}\Big] \qquad \mathcal{S}_{\theta,SL} = \gamma(z)\,\left[\theta(\mathbf{x}) - \left(\theta_0 + (z - z_i^1)\frac{\mathrm{d}\langle\theta\rangle}{\mathrm{d}z}\right)\right] \tag{5.4}$$

Two simulation domains are considered depending on the application:

- **Grid $\mathbf{128^3}$**: C: $128 \times 128 \times 128$ (+40) P: 4000 [m] $\times$ 4000 [m] $\times$ 2400 (+750) [m]
- **Grid $\mathbf{128 \times 256^2}$**: C: $256 \times 256 \times 128$ (+40) P: 4000 [m] $\times$ 4000 [m] $\times$ 2400 (+750) [m]

with P and D respectively referring to the Computational (ie: $N_x \times N_y \times N_z$) and Physical (ie: $L_x \times L_y \times L_z$) domains. The numbers between brackets indicate the dimensions of the sponge layer. In both cases, a sponge spanning roughly 25 % of the vertical domain is applied. Both grids also result in the same spacial resolution:

$$\Delta_x \times \Delta_y \times \Delta_z = 31.25\,[\mathrm{m}]\ \times 31.25\,[\mathrm{m}]\ \times 18.75\,[\mathrm{m}] \tag{5.5}$$

The flow is thus resolved down to smaller scales with those grid than with the one used by Schmidt & Schumann and a finer spacial resolution is used in the wall normal direction z. The resulting numerical setup is best illustrated by Fig. 5.1.

	Schmidt & Schumann	**BigFlow**
Top BC	Radiation BC	Sponge Layer
Lateral BC	Symetry	
Lower BC	Monin-Obukhov similarity theory with constant heat flux	
SGS Model	TKE Based	Smagorinsky and constant Pr_{SGS}
Initial conditions	Mixed layer topped by a strong inversion layer and random velocity and temperature fluctuations	Same but surface layer initialized to non zero velocity
Computational domain	$160 \times 160 \times 48$	$128 \times 128 \times 128$ (+40) $256 \times 256 \times 128$ (+40)
Physical domain	8000 [m] $\times$ 8000 [m] $\times$ 2400 [m]	4000 [m] $\times$ 4000 [m] $\times$ 2400 (+750) [m] 8000 [m] $\times$ 8000 [m] $\times$ 2400 (+750) [m]

Table 5.1: Comparison of the numerical setups used in this thesis to that of Schmidt & Schumann

A final adjustment is made to the initial conditions. The horizontal velocity of the first layer is set to a random small yet non zero fluctuating initial value to avoid bad behavior of the law of the wall at the first time step (ie: zero horizontal velocity magnitude in Eq. (4.21)). Table 5.1 sums up the differences between the two setups in a more visual way.

5.2 Validation of the results and tuning of the coefficients

This Section aims at validating the code implemented in the context of CBLs. The results are compared to the one of Schmidt & Schumann both in term of mean profile and in term of wavenumber spectra. We then investigate the effects of the sponge layer and of the turbulent Prandtl number choice on the system.

5.2.1 Comparison of the profiles

The integration is carried from the initial conditions until quasi-steady state at $t_* = 6$ ($t = 65000$ [s]). The largest domain is used (ie: $8000\,[\mathrm{m}] \times 8000\,[\mathrm{m}] \times 2400\,(+750)\,[\mathrm{m}]$). The resulting spacially averaged profiles are depicted on Figs. 5.3-5.7. The $(\cdot)'$ indicates fluctuations in the Root-Mean-Square sense (ie: $\phi'(z) = \left((\phi - \langle\phi\rangle)^2\right)^{1/2}$) while the $\langle\cdot\rangle$ operator denotes an horizontal average. The profiles are adimensionalized using the convective scales previously defined (*cfr:* : 2.3). The results obtained using BigFlow are compared to these of Schmidt & Schumann and to laboratory measurements collected by Deardorff & Willis [38] and Willis & Deardorff [39].

The evolution height of the inversion layer plotted on Fig. 5.2 ($\mathrm{Pr}_{SGS} = 0.5$) allows to perform a first diagnostic of the results obtained. Schmidt & Schumann suggest that the height of the inversion layer increases roughly linearly with time:

$$\frac{z_i^n}{z_i^{ref}} = 0.875 + 0.0221\ t_* \tag{5.6}$$

Our results lead to a similar conclusion regarding the growth rate of the inversion layer ($z_i^n / z_i^{ref} = 0.8390 + 0.0229 t_*$). Yet the starting height of the inversion layer is lower in our case. This would suggest an error in the formulation of the initial conditions. The topic was investigated but unfortunately without success. However the fact both modeld exhibit the same growth rate at least partly validates our results.

The dimensionless spatially averaged temperature profiles $\langle\theta\rangle/\theta_C^{\mathrm{ref}}$ is provided by Fig. 5.3. The profiles were adimensionalized with the reference inversion height, z_i^{ref}, to ensure a fair comparison. The initial temperature is also plotted for reference. The results computed using BigFlow are in close agreement with the ones of Schmidt & Schumann . However our results slightly deviate from that of Schmidt & Schumann near the wall and in the entrainment layer. The deviation at the bottom of the domain might be explained by the use of different types of boundary conditions. A shallow super-adiabatic ($\partial\theta/\partial z < 0$) layer is formed at the bottom of the domain due to the radiation heating from the underlying ground and the absence of mean horizontal wind. This absolutely unstable layer of air is topped by the mixing layer which roughly spans heights $z/z_i^6 = 0.05$ to 0.95. The later is characterized by an almost constant temperature due to the intense turbulent mixing. This can be seen as an indicator quasi-steady state is reached. In contrast Fig. 5.8 shows that at the beginning of the simulation the turbulent structures are not fully developed. As a result, non-uniform values of the temperature profile across the mixed layer are obtained at the beginning of the time integration (ie: higher temperature at the bottom). The mixing layer progressively develops until the rise of thermals is stopped by the stable inversion layer. At this point the turbulent structures are fully developed.

Fig. 5.4 depicts the evolution of the normalized vertical turbulent heat flux $\langle\theta' w'\rangle/\theta_C^{6.5} w_C^{6.5}$. Overall both curves predict the same behavior but do not agree on the exact values. BigFlow tend to underestimate the vertical heat flux compared to Schmidt & Schumann . Yet the curve computed using BigFlow is in better agreement with the experimental results. The vertical turbulent heat flux decreases almost linearly with height up to the turbulent layer where it reverses. The temperature increase rate thus remains almost uniform across mixed layer.

The evolution of the mean temperature fluctuations $\langle\theta'^2\rangle/(\theta_C^6)^2$ is illustrated on Fig. 5.7. The results computed match both Schmidt & Schumann ones and the experimental data. The average temperature fluctuations magnitude decreases with height in the mixed layer where the temperature is almost uniform. It then starts increasing again in the entrainment region.

In Figs. 5.5 and 5.6, the variance of the three different velocity components, $\langle u^2\rangle/(w_C^{6.5})^2$, $\langle v^2\rangle/(w_C^{6.5})^2$ and $\langle w^2\rangle/(w_C^{6.5})^2$, are plotted against the normalized height $z/z_i^{6.5}$. Once again the general shapes of the profiles match fairly well those of Schmidt & Schumann though the exact values they predict slightly differ. Willis & Deardorff's experimental data on the other hand predicts much higher values of the horizontal variances. This problem was already investigated by Schmidt & Schumann who concluded the experimental setup itself was likely to be the cause of those differences [9]. The variance of the horizontal velocity components is generally lower than that of the vertical component except at the edges of the mixed layer where the opposite tendency appears. Vertical velocity fluctuations are primarily caused by buoyancy while only the lower local pressure gradients are driving the horizontal motions. One therefore expects the horizontal velocity variance to be lower than the vertical one [9]. Close to the wall and in the entrainment layer, the tendency reverses. Horizontal fluctuations become predominant. To end with, we should also note that the deviation observed between to u and v fluctuation profiles seem to be inconsistent with the horizontal homogeneity assumption.

The code developed was thus tested against standard atmopsheric CFD benchmark data and experimental data with success. The values computed remain quite close from the ones obtained by Schmidt & Schumann and both models predicts the same behavior of the flow. The initial offset in the starting height of the inversion layer appear to preserve the characteristics of the flow and is therefore not critical. Nonetheless some difference can still be observed which is expected as both codes rely on slightly different setups not only in term of boundary conditions but also in term of modelization of the SGS term.

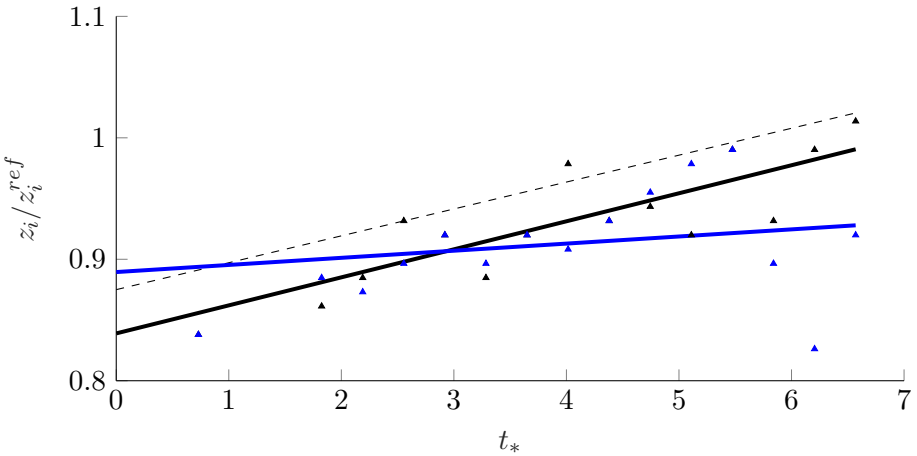

Figure 5.2: Evolution of the dimensionless height of the inversion base, z_i^n/z_i^{ref}, with the dimensionless time for $\mathrm{Pr}_{SGS} = 0.75$ (blue) and 0.5 (black). Thick dark line: evolution of the dimensionless height of the inversion base linearly interpolated from the data retrieved from BigFlow (markers). Black thin dashed line represents the evolution predicted by Schmidt & Schumann

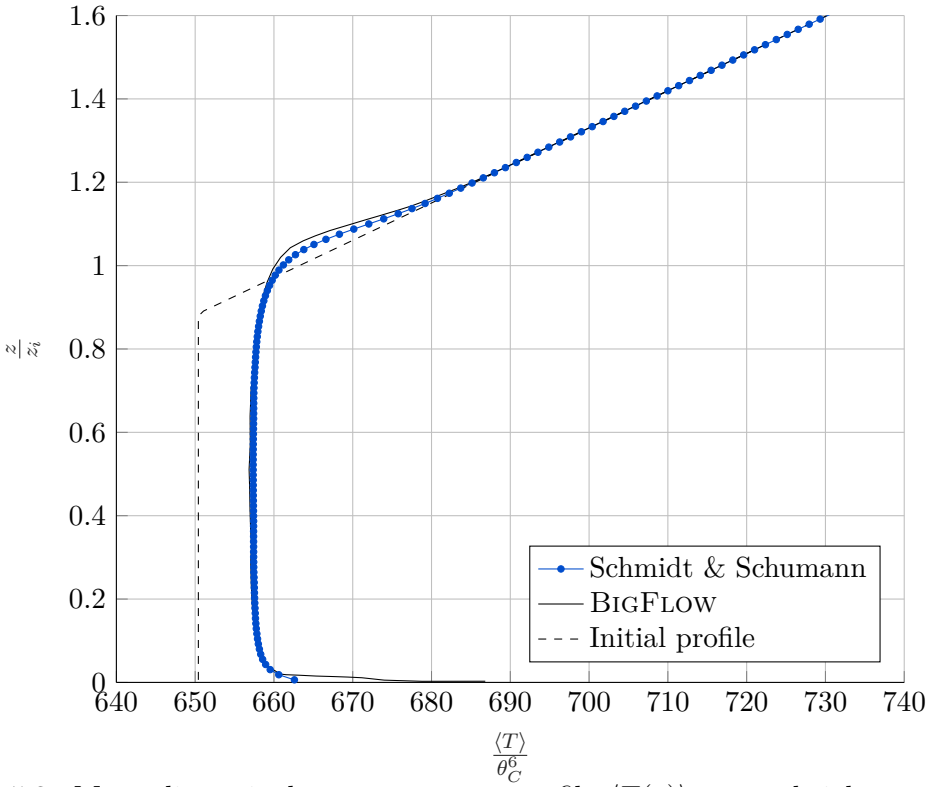

Figure 5.3: Mean dimensionless temperature profile $\langle T(z) \rangle$ versus height at $t_* = 6$ - results obtained using BigFlow compared to Schmidt & Schumann results

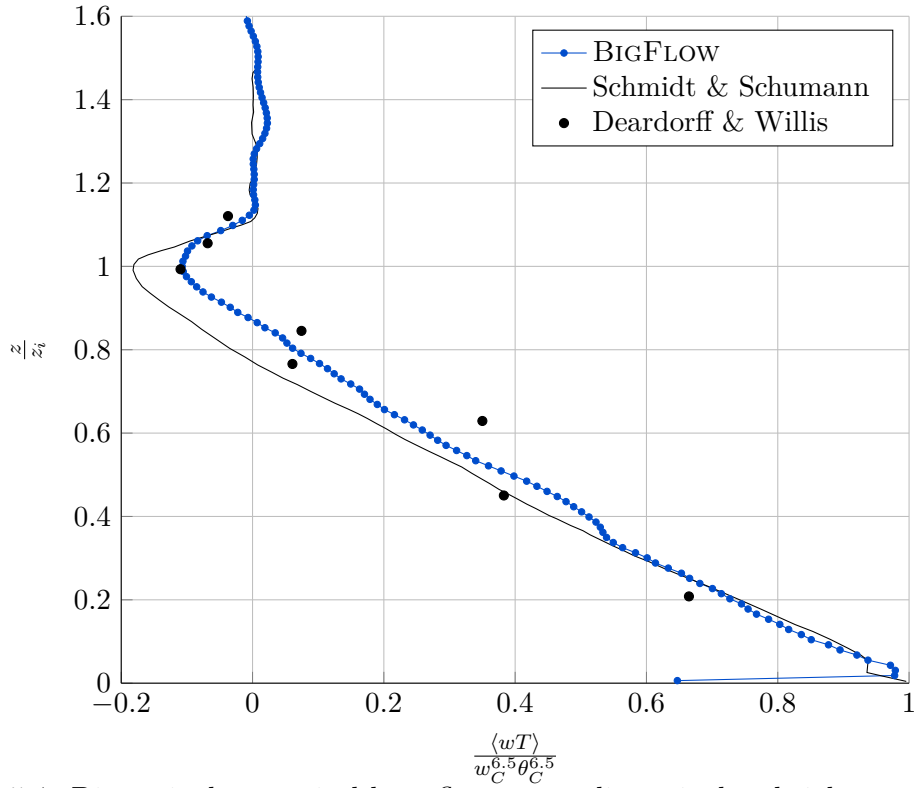

Figure 5.4: Dimensionless vertical heat flux versus dimensionless height at $t_* = 6.5$ - results obtained compared to Schmidt & Schumann results and to laboratory measurements of Deardorff & Willis [38]

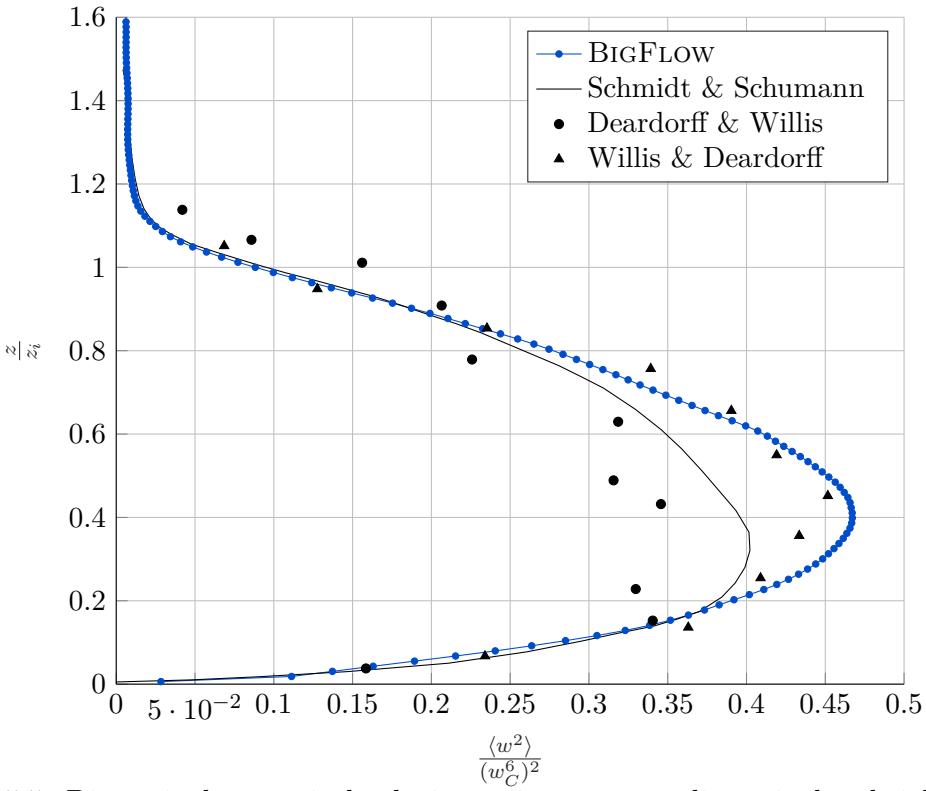

Figure 5.5: Dimensionless vertical velocity variance versus dimensionless height at $t_* = 6.5$ - results obtained compared to those of Schmidt & Schumann and to laboratory measurements of Deardorff & Willis [38] and of Willis & Deardorff [39]

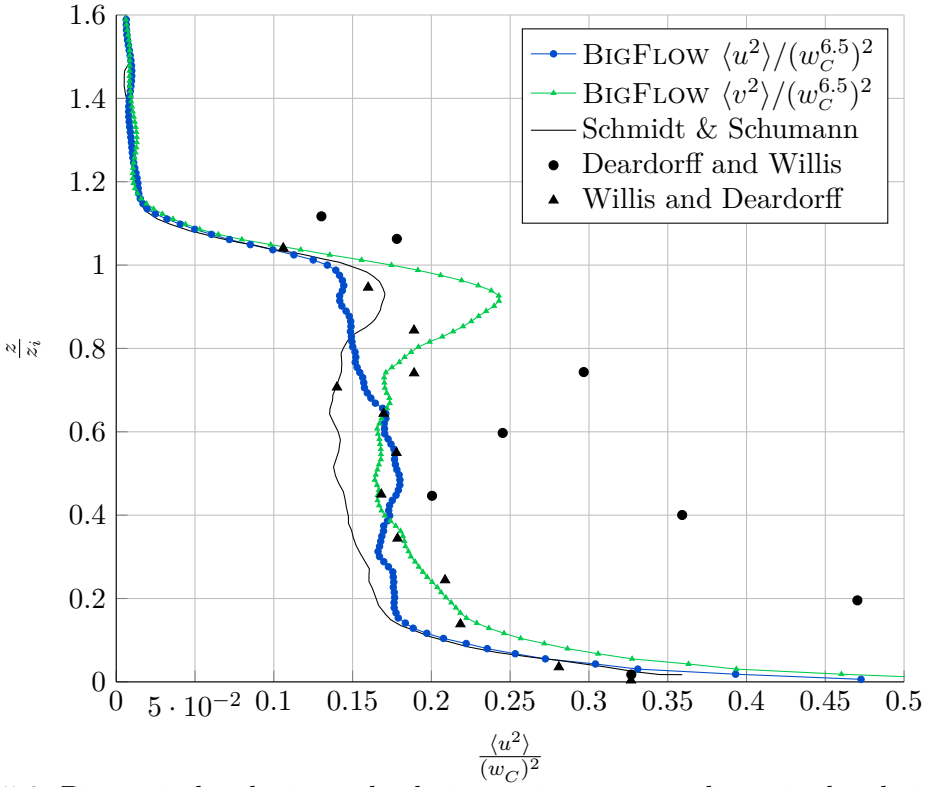

Figure 5.6: Dimensionless horizontal velocity variance versus dimensionless height at $t_* = 6.5$ - results obtained compared to those of Schmidt & Schumann and to laboratory measurements of Deardorff & Willis [38] and of Willis & Deardorff [39]

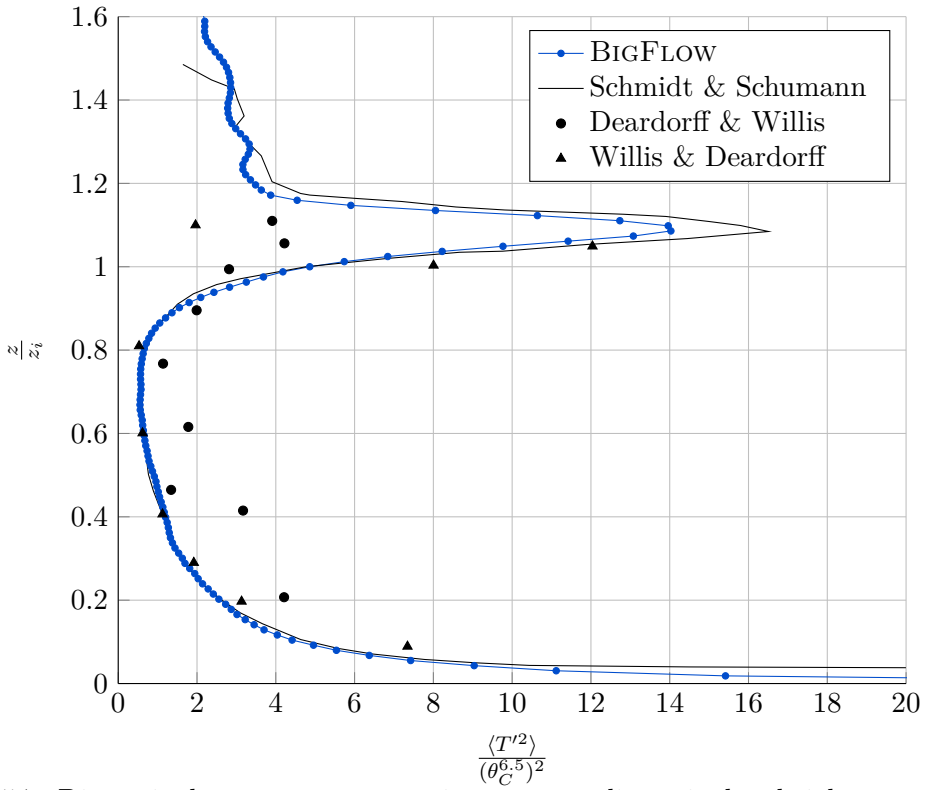

Figure 5.7: Dimensionless temperature variance versus dimensionless height at $t_* = 6.5$ - resulted obtained compared to those of Schmidt & Schumann and to laboratory measurements of Deardorff & Willis [38] and of Willis & Deardorff [39]

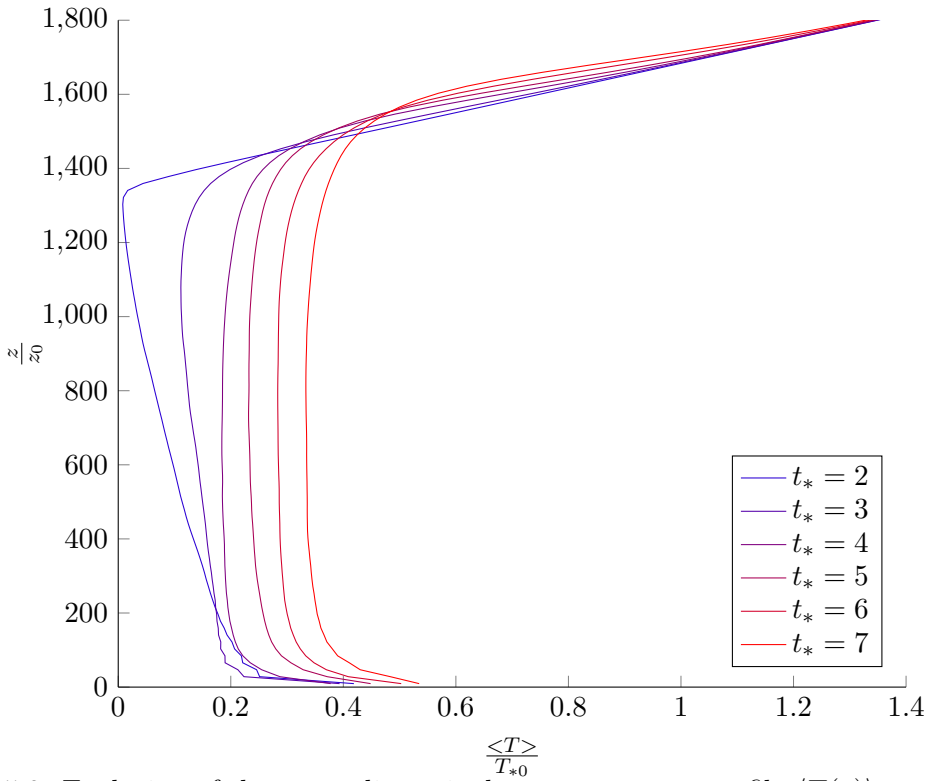

Figure 5.8: Evolution of the mean dimensionless temperature profile $\langle T(z) \rangle$ versus height from $t_* = 2$ to $t_* = 7$

5.2.2 Spectral analysis

The power density spectra allows to highlight the contribution to the total production of TKE per wavenumber bin, thereby evaluating the relative importance of the different scales. Fig. 5.9 depicts the normalized compensated spectra at dimensionless time $t_* = 6$ and at various dimensionless height z/z_i^6. For an arbitrary fluctuating quantity ϕ, the energy density spectra reads [3]:

$$E_\phi(k_i) = \frac{4\pi}{NF_s}\left|\hat{\phi}_i\right|^2 \tag{5.7}$$

with i, the wavenumber index, $i = 0, ..., N/2$, N being the number of samples provided at the sampling frequency F_s. $\hat{\phi}_i$, the Fourier coefficients of the discrete space signal ϕ are determined using a standard Fast Fourier Transform algorithm. The spectra are computed along parallel horizontal lines and then averaged over the corresponding plane (ie: Oxy). E_u, E_w, E_θ denote respectively the vertical velocity, horizontal velocity and potential temperature energy density spectra. The spectra are further multiplied by the wave number k and then normalized by the associated convective scale to obtain the compensated power density.

As stated previously, Large Eddy Simulation do not resolve all scales explicitly The smallest scales are modeled using the SGS parametrization while only the largest scales are resolved explicitly. The truncation can however not be performed anywhere. Classical SGS turbulence closure theory relies on the cut being made well within the inertial subrange, between the integral

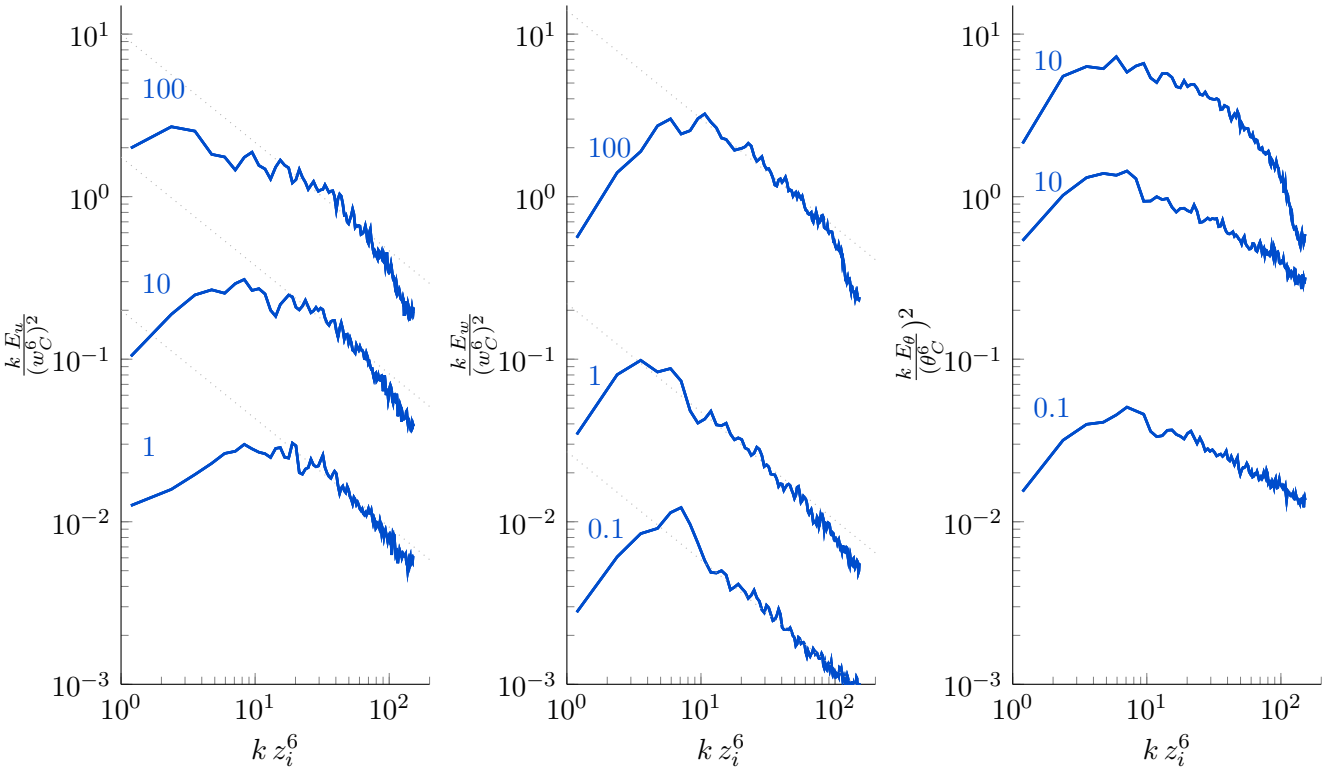

Figure 5.9: Normalized horizontal power density spectra of the horizontal velocity component, kE_u/w_C^6, vertical velocity component, kE_w/w_C^6, and temperature, kE_θ/θ_C^6, at time $t_* = 6$ versus the dimensionless wave number kz_i^6. Spectra plotted at different dimensionless height: $z/z_i^6 = 0.21$, 0.61 and 0.98 respectively (from top to bottom). To avoid overlapping, the results were offset by a constant factor (ie: 0.1, 1, 10, 100). The -2/3 slope corresponding to the Kolmogorov inertial subscale is plotted in dashed line

scale and the Kolmogorov microscale [40]. In the inertial subrange, Kolmogorov's spectrum theory states that [9]:

$$E_u(k) \propto \langle\epsilon\rangle^{2/3} k^{-5/3}, \qquad E_w(k) \propto \langle\epsilon\rangle^{2/3} k^{-5/3}, \qquad E_\theta(k) \propto \langle\epsilon_\theta\rangle\langle\epsilon\rangle^{-1/3} k^{-5/2} \tag{5.8}$$

with ϵ the dissipation rate. The inertial subrange is thus associated with a $-2/3$ slope in the normalized compensated spectra *loglog* diagram . As expected, we can see that the -2/3 spectral behavior is indeed present in the spectra computed (in dotted lines in Fig. 5.9) which further validate our results.

The normalized energy density profiles obtained were also compared against those of Schmidt & Schumann (not plotted here) and were overall similar. The overall shapes of the profiles are quite resemblant notably with both setups resulting in roughly the same peak wave number. Only the potential temperature spectra were found to be a little underdissipative at high wavenumber compared to the ones obtained by Schmidt & Schumann . Once again, differences are expected, especially given the fact a constant Pr_{SGS} is used in our simulation while Schmidt & Schumann rely on a TKE prognostic equation closure model. The spectral power density can further be used to highlight the respective contribution of each wavenumber bin to the total TKE production and hence better understand the physics of the problem. One would expect the contribution of the small scales to increase as the flow gets closer to the ground. We can indeed see the relative importance of the high wave number mode decreases with height. The wavenumber peak slightly shift to the right as we get further way from the ground. Moreover, we can also see that the maximum power density is observed for kz_i^6 $\mathcal{O}(7)$ which roughly corresponds to motions with the height of the mixed layer as a characteristic size. This also sugests that using a reduced domain (ie: Grid 128^3 with $4000\,[\mathrm{m}] \times 4000\,[\mathrm{m}] \times 2400\,(+750)\,[\mathrm{m}]$) will not enable us to correctly capture the large eddies. Various runs were performed to asses whether or not the peak wavenumber is effectively captured with the reduced domain. This lead to the conclusion that the reduced domain is not sufficient to correctly capture the wavenumber peak especially close to the ground. Yet it predicts correctly the spectra across the inertial subrange compared to the full domain.

Following the computation of the horizontally averaged statistics we moved on to checking the associated power density spectra were consistent. The results were found to be similar to that of Schmidt & Schumann . They were further validated by the of the -2/3 power law. Moreover we showed the peak frequency was captured by the larger grid while more caution is needed regarding the accuracy of the smaller one.

5.2.3 Impact of the sponge layer parametrization

As mentioned previously the calibration of the sponge layer is a tricky process. An appropriate selection of the damping constant, γ_d, is crucial. Indeed excessive values lead to reflexion while insufficient values make the sponge essentially useless. The tuning of this coefficient is case dependent. It is influenced by many factors among which the depth of the absorbing layer and the intensity of the heat flux.

In order to determine the value of this coefficient in the case studied, various runs were performed with different damping coefficients: $\gamma_d = 0.001, 0.01$ and 0.1 $[\mathrm{s}^{-1}]$ respectively. The results were compared to the ones of another run where no sponge layer was applied but where the total depth of the domain was kept identical (ie: corresponds to $\gamma_d = 0.0$ $[\mathrm{s}^{-1}]$ and $L_z = 2400$ $(+750)$ [m]). Indeed, using a reduced domain (ie $L_z = 2400$ [m]) along with a rigid lid boundary at the top would not have guaranteed a fair comparison. It would not have been possible to establish whether the changes observed were due the effect of the sponge layer itself or to the extended domain it required. The simulations were run starting from the initial conditions until quasi-steady state was reached using the 128×256^2 grid.

Fig. 5.10 depicts the mean RMS fluctuation profiles obtained for all four simulations. As expected, we observe that the higher the damping constant, the faster the fluctuations are eliminated. An absorbing layer with insufficient damping is useless. Fluctuations reach the wall nearly undamped. Both $\gamma_d = 0.001$ [s^{-1}] (thin black line) and 0.0 [s^{-1}] (thick black line) consequently exhibit roughly the same behavior. Conversely, $\gamma_d = 0.1$ [s^{-1}] (blue dashed line) might also lead to high reflection even though fluctuations are effectively damped before they reach the near wall region. Indeed, the initial section of the damped profile for $\gamma_d = 0.1$ [s^{-1}] ($z/z_i = 1.5 - 1.6$) is similar to that observed at the wall for the undamped case. This could suggest that the sponge layer behaves like a semi-permeable wall due to its excessive damping coefficient thus reflecting a large part of the incoming waves.

The power density spectra associated to an arbitrary fluctuating variable ϕ is attenuated by the sponge. The associated power density spectra ratio expressed in decibels reads:

$$\mathcal{A}_\phi(z) = 10 \log \left(\frac{E_\phi(k, z)\, k}{E_\phi(k, z_{SL})\, k} \right) \tag{5.9}$$

where $E_\phi(k, z)$ is the energy density spectra of variable ϕ at height z with z_{SL} the reference height (ie: the bottom of the sponge layer).

Clearly, the setup already strongly damps the vertical velocity component and potential temperature fluctuations even without any sponge layer (*cfr:* Fig. 5.11). Indeed the minimal attenuation for both fields already reaches a minimum (in absolute value) value of -20 dB in that case. This implies that strong statically stable inversion layer already filters out a large part of the fluctuations by itself. The horizontal velocity fluctuations, on the other hand, appear to remain

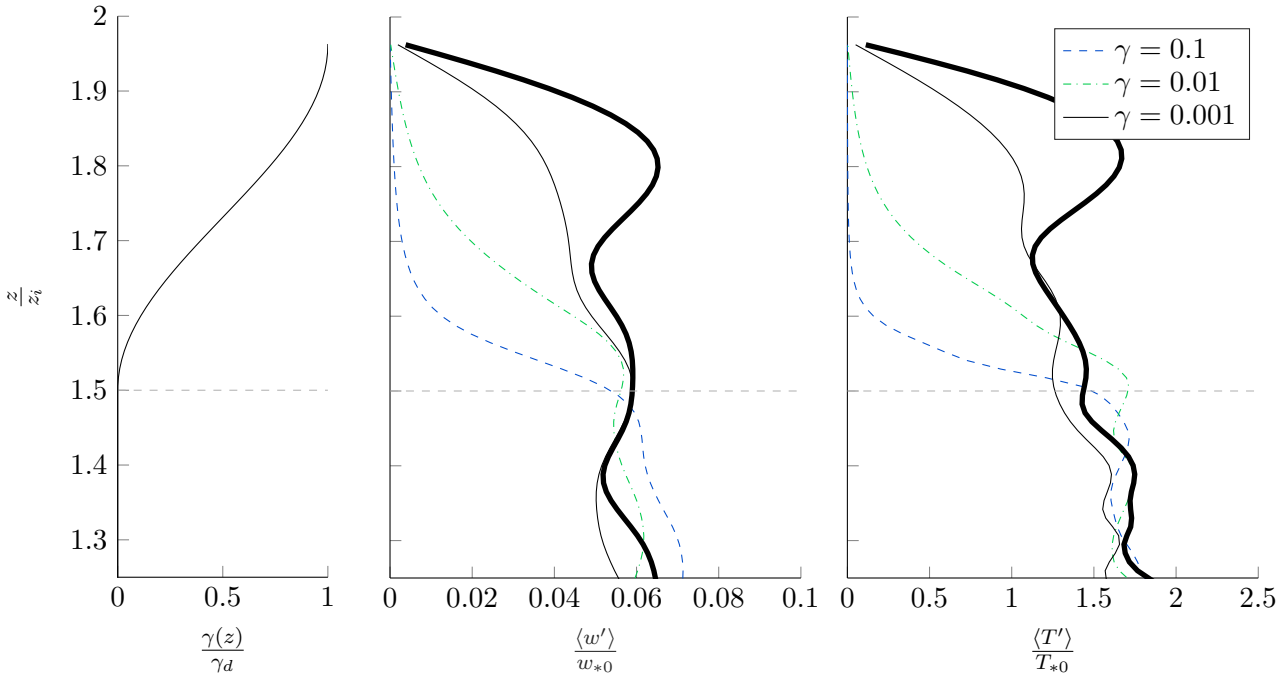

Figure 5.10: Evolution of the dimensionless RMS fluctuation profiles of the mean vertical velocity component $\langle w' \rangle / w_C^6$ and potential temperature $\langle \theta' \rangle / \theta_C^6$ through the sponge layer for different damping coefficients $\gamma_d = 0.001, 0.01$ and 0.1 [s^{-1}]. Profiles plotted at quasi steady state: $t_* = 6$ and compared to the case with no sponge layer (thick line): $\gamma_d = 0$ [s^{-1}]. Bottom of the sponge layer indicated by the horizontal dashed line

nearly unaffected by the damping effect provided by the inversion layer and consequently remain roughly constant trhough the inversion layer. The lowest damping coefficient (ie: $\gamma_d = 0.001$ [s^{-1}]) only results in a minor increase ($\mathcal{O}(-5dB)$) in power density spectra attenuation ratio. As noted previously, further increasing the damping constant logically leads to even higher attenuation ratio values and hence faster damping. We should also note that, in all three cases, the damping is not uniform over all wave numbers. Wavenumber ranging from $kz_i^6 \sim 10$ to 15 undergo the strongest damping.

Following those constatation, the damping constant is somewhat arbitrarily set to $\gamma_d = 0.005$ [s^{-1}]. This value should provide sufficient attenuation of the fluctuations while still being low enough to make sure the sponge layer does not simply reflect the incoming waves. Yet the question remains: is the sponge actually affecting the flow statistics computed and the physic of the problem. Indeed, up to now, no evidence that the sponge layer effectively improves the physics of the problem was found.

Fig. 5.12 allows to compare the power density spectra retrieved from the different simulations performed. No obvious difference can be spotted between the spectra, they look relatively alike. This suggests the sponge layer is not necessary in the case studied. This conclusion is further validated by the intercomparison of the horizontally averaged statistics. They were compared against the Schmidt & Schumann reference profiles with the same degree of success dependless on the damping coefficient chosen (not plotted). The sponge layer thus does not appear to effectively impact the solution in the case treated.

In the context ABL modeling, sponge layers are primarily used to deal with flows over large mesoscales obstacles such as mountains or ridges. The resulting mountain waves can propagate up to very high altitudes which makes the formulation of a radiation or absorbing boundary condition absolutely necessary to avoid reflexion of the induced gravity waves against the top of the domain. This topic is extensively studied in the literature and various types of boundary condition are investigated (eg: [41]). As mentioned previously, many authors also argue that similar types of boundary conditions should be applied to convective boundary layer. However many evidences of authors getting away with simply considering a rigid boundary condition can be found (eg:[21][42]). The formulation of a specific boundary condition thus does not appear to be always required depending on the convection regime and the vertical extent of the simulated domain.

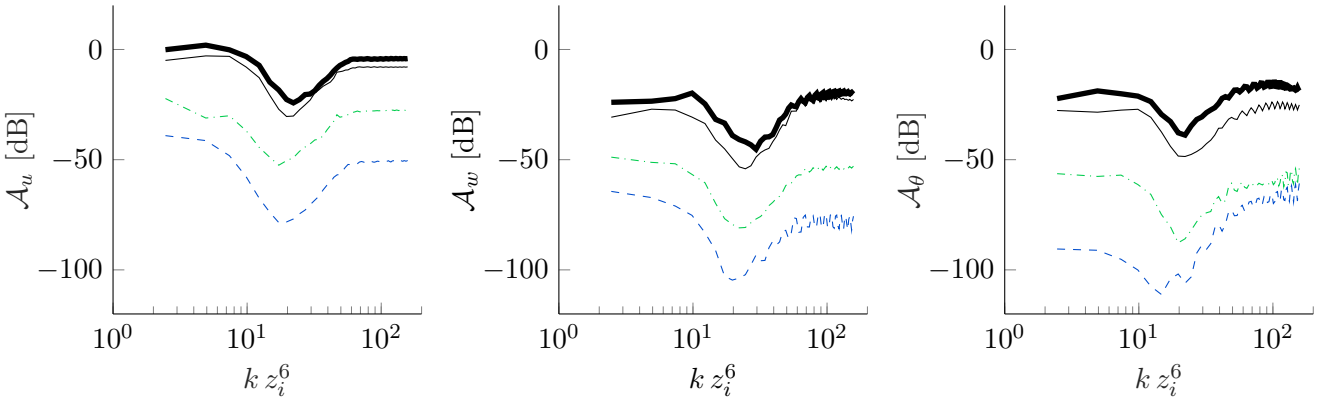

Figure 5.11: Ratio of the power density spectra at the lower edge of the sponge layer z_{SL} and at the upper edge of the domain z_{top} at dimensionless time $t_* = 6$ expressed in dB and as a function of the dimensionless wave number kz_i^6. Thick black line: no sponge layer, Full black line: $\gamma_d = 0.001$ [s^{-1}], dash-doted green line: $\gamma_d = 0.01$ [s^{-1}] and dashed blue line: $\gamma_d = 0.001$ [s^{-1}]

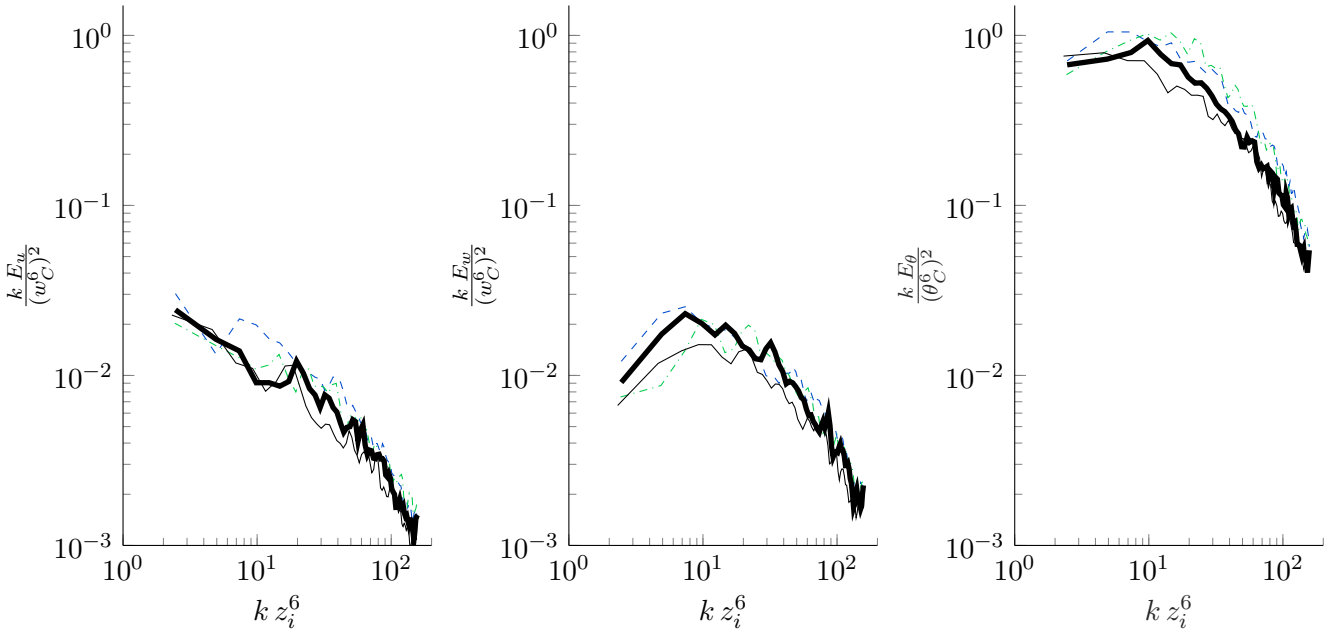

Figure 5.12: Normalized horizontal power density spectra of the horizontal velocity component, $k\phi_u/(w_C^6)^2$, vertical velocity component, $k\phi_w/(w_C^6)^2$, and temperature, $k\phi_\theta/(\theta_C^6)^2$, and for various values of the damping constant. results plotted at time $t_* = 6$ versus the dimensionless wave number kz_i^6. Color as defined previously: thick black line, $\gamma_d = 0.0$ [s^{-1}]; thin black line, $\gamma_d = 0.001$ [s^{-1}]; dash-dotted green line, $\gamma_d = 0.01$ [s^{-1}] and dotted blue line, $\gamma_d = 0.1$ [s^{-1}]

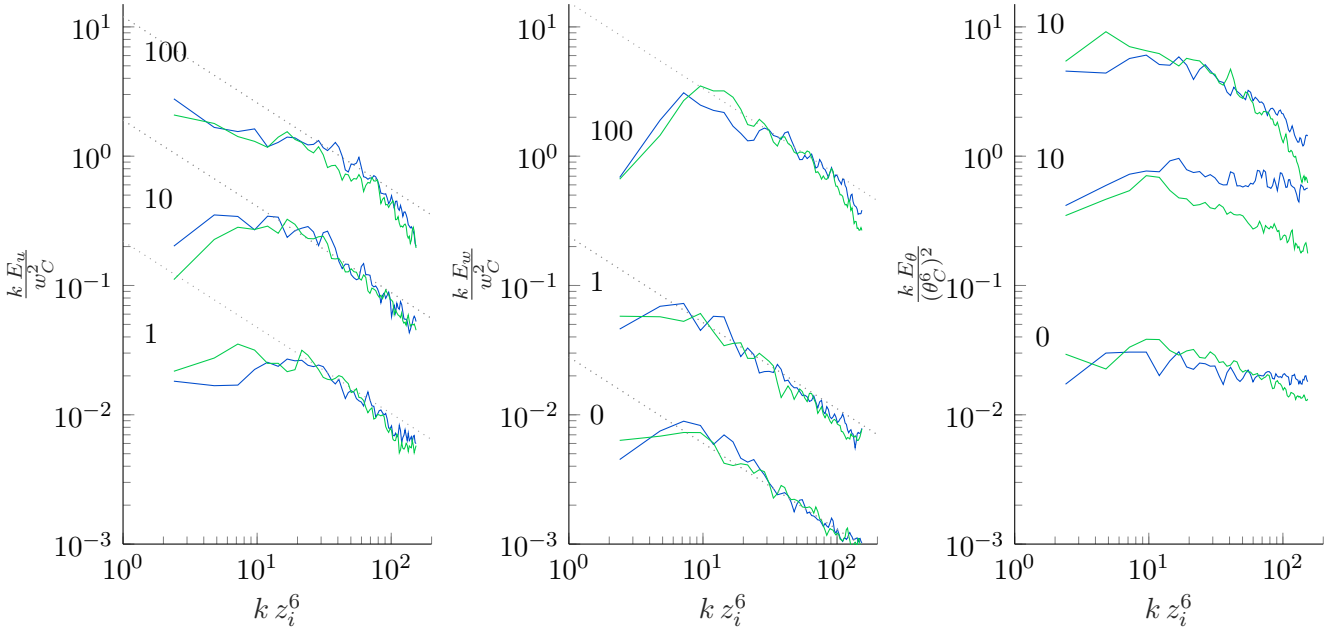

Figure 5.13: Normalized horizontal power density spectra of the horizontal velocity component, $k\phi_u/(w_C^6)^2$, vertical velocity component, $k\phi_w/(w_C^6)^2$, and temperature, $k\phi_\theta/(\theta_C^6)^2$, and for various values of the damping constant. Results plotted at time $t_* = 6$ versus the dimensionless wave number kz_i^6. Green line: $\mathrm{Pr}_{SGS} = 0.5$ and blue line $\mathrm{Pr}_{SGS} = 0.75$

5.2.4 Impact of the SGS Prandtl number

In standard Engineering application, the Pr_{SGS} can be chosen as high as 0.7. The values used in the context of ABL modeling are considerably lower. As indicated previously most authors seem to agree on value ranging from 0.4 to 0.5. The effect of the SGS Prandtl number on the flow was thus investigated and is presented in this Section. The results are computed using the same smaller grid (Grid 128^3) from the initial condition and until quasi-steady state is reached. The same procedure as presented previously is then applied to retrieve the normalized horizontal power density profiles.

Fig. 5.13 compares normalized horizontal power density profiles retrieved from the two simulations performed. Compared to our previous results who showed good agreement with that of Schmidt & Schumann , the results obtained with $\mathrm{Pr}_{SGS} = 0.75$ lead to a loss of accuracy associated to an over evaluation of the contribution of small scales. This phenomenon is to be expected if we recall that $\alpha_{SGS} = \nu_{SGS}/\mathrm{Pr}_{SGS}$. The effective diffusion coefficient $((\alpha + \alpha_{SGS}))$ thereby decreases with results in temperature fluctuations not being smoothed out as they should. This in term drive their overall contribution to the flow up, consequently increasing the relative contribution of the high wave number bins. The velocity spectra on the other hand appear to remain relatively unaffected by this change change of Pr_{SGS} even though they are directly coupled to the temperature field via the buoyancy term.

Generally speaking, when plotted in term of the dimensionless height z_i^6, the statistics obtained in both cases are quite similar (no plotted here). In fact, the profiles themselves do not change much but their vertical extent is significantly affected by the variations of the SGS Prandtl number. Higher Pr_{SGS} lead to the formation of a shallower mixed layer. This phenomenon was previously illustrated by Fig. 5.2. On that Figure, one can indeed see that, higher values of Pr_{SGS} translate into a slower ascending rate of the inversion layer.

5.3 Three dimensional structure of the CBL at quasi steady state

Up to now our study of the convective boundary layer has mostly been limited to that of two dimensional mean profiles. Although this approach is convenient to validate the results and develop a preliminary idea of the flow structure it is of limited use to describe the full three dimensional structure of the flow. Figs. 5.14 to 5.16 allow to better picture the overall structure of the CBL modelled. The later is very similar to that described by Schmidt & Schumann [9] and Garratt [1] in their respective works.

Fig. 5.14 depicts a vertical xz cut of the domain taken at $y/z_i^6 = 0$. The top cross section illustrates the instantaneous temperature and velocity fields at $t_* = 6$ while the bottom one represents the same field but averaged over one convective time from $t_* = 6$ to 7. Two updraughts are clearly visible in that slice of the domain. Generally speaking, narrow *updraughts* with relatively high vertical velocities (ie: maximum speed of around 3 $[\mathrm{ms}^{-1}]$ at $z/z_i^6 = 0.75$) are surrounded by broad areas of slowly sinking air, the *downdraughts*. Buoyant updraughts find their origin in the thin super adiabtic layer formed just above the surface due to the radiative heating provided by the ground. *Isolated plumes* rising in areas remote from strong updraft are highly unstable and are rapidly destroyed by the counteracting effect of the downdrafts. Conversely, if several plumes are sufficiently close to each other to merge, they can end up forming a larger scale column associated with a strong updraft that can possibly extend up to the inversion layer. This is better illustrated by Fig 5.15. Two large updraft convergence zones are visible within the subdomain considered. We see that the plumes around that convergence zone tend to merge together thereby creating large coherent structures extending up to high altitude. Outside these two convergence zones, only a few narrow structure are discernable.

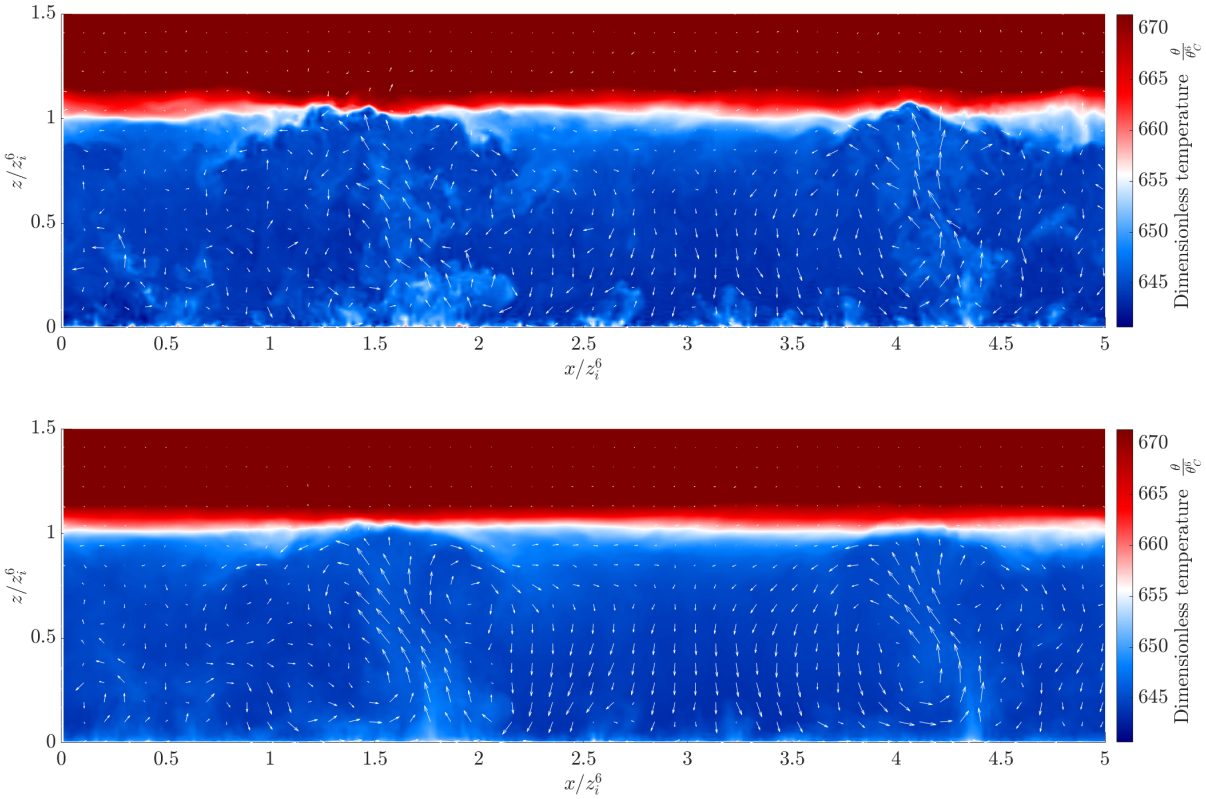

Figure 5.14: **Top:** Oxz cross section ($y/z_i^6 = 0$) of the domain at $t_* = 6$ - Quiver plot: instantaneous velocity field - Contour plot : instantaneous dimensionless temperature field **Bottom:** Oxz cross section ($y/z_i^6 = 0$) of the domain temporally averaged from $t_* = 6$ to 7 - Quiver plot: temporally averaged velocity field - Contour plot: temporally averaged dimensionless temperature field

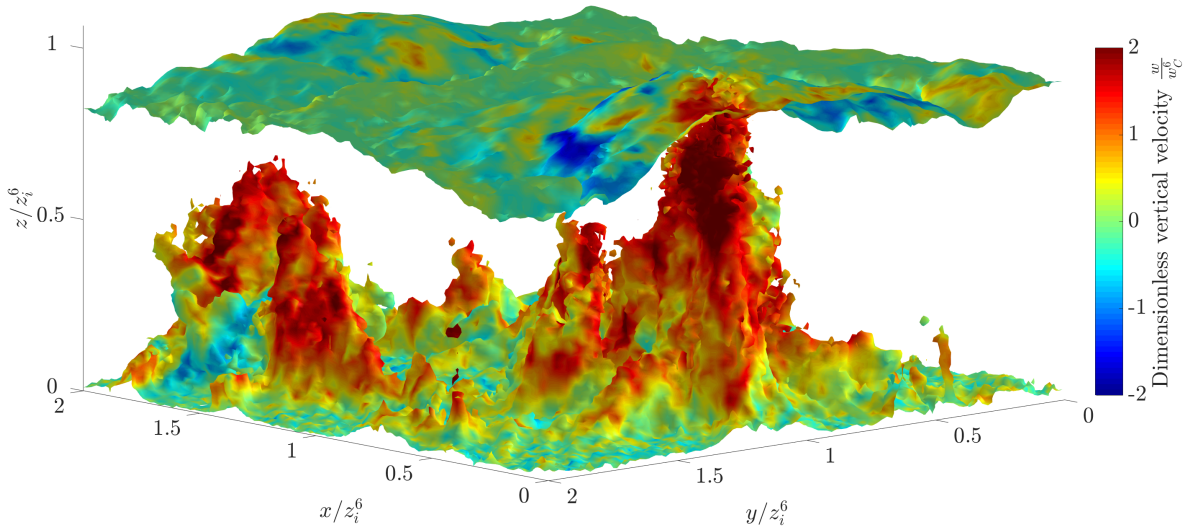

Figure 5.15: **3D isosurface:** $\theta/\theta_C^6 = 718$ ($\theta = 300.1$ [k]) averaged over a convective time from $t_* = 6$ to 7. **Color map** corresponds to the mean dimension vertical velocity component w/w_C^6. Results represented only in the subdomain $x/z_i^6 \in [0,\ 2]$ and $y/z_i^6 \in [0,\ 2]$

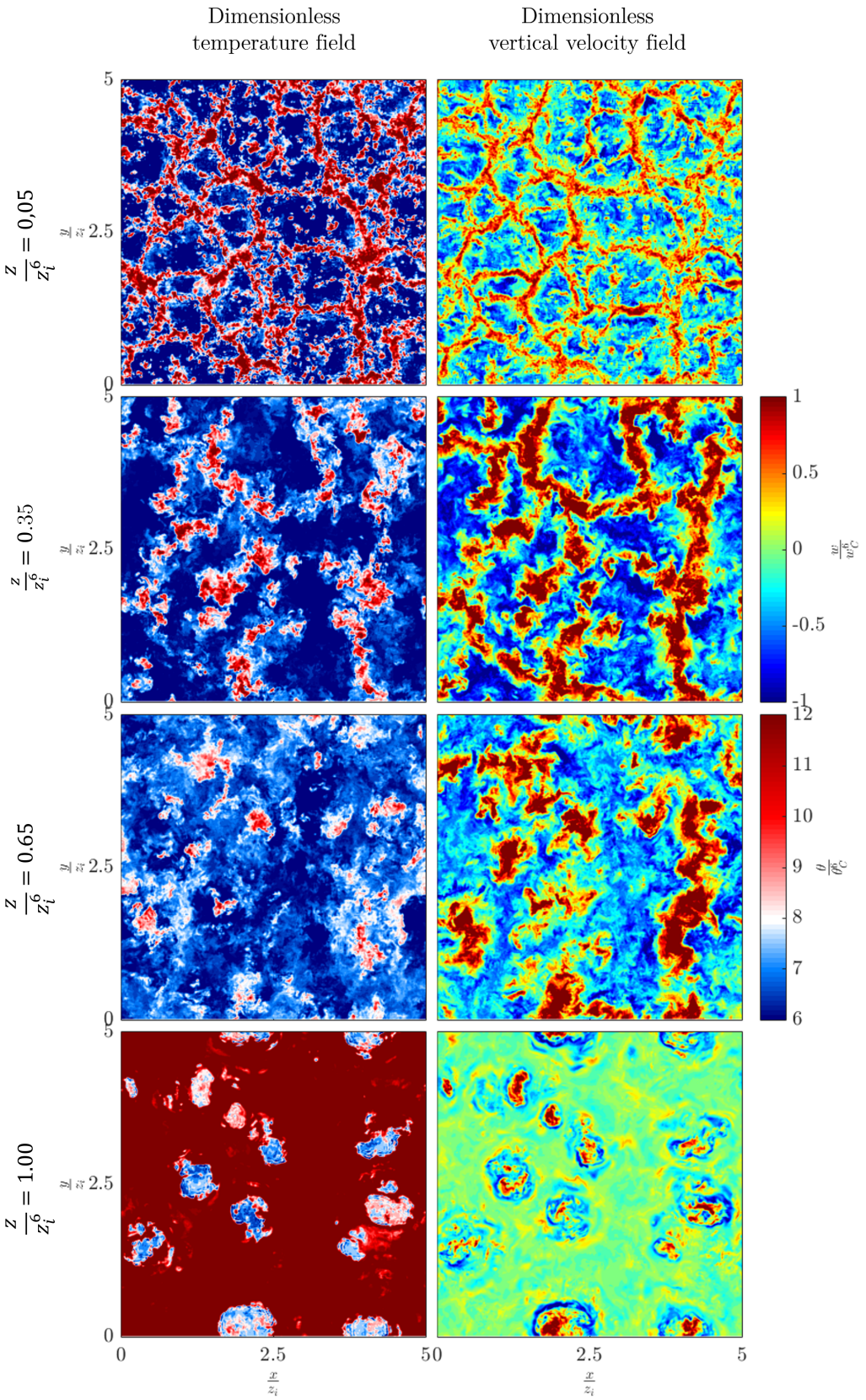

Figure 5.16: Horizontal contour plot in the Oxy plane of the dimensionless temperature fluctuations θ'/θ_C^6 (**left**) and vertical velocity (**right**) at dimensionless time $t_* = 6$. Contour plotted at different heights: $z/z_i^6 = 0.05,\ 0.35,\ 0.65$ and 1.00.

As a result of turbulent mixing, the temperature variations of the environment tend to slowly disappear with altitude which implies the average temperature of the plumes will decrease as they rise. The largest scale plumes continue to ascend until they encounter the strong static inversion layer. At this height, further vertical motion is prevented by the inversion layer. Consequently the incoming flow spreads outwards and returns as descending air in the downdraft region. Part of the flow penetrates in the inversion layer by turbulent motions. This phenomenon is referred to as the *entrainment* process. It is formally defined as [1] "*the process whereby miscible fluid is exchanged across a density interface bounding a turbulent region*" (ie: the inversion base). This transfer of fluid results in destruction of TKE and in *dome-like local deformations* of the inversion base. The subsequent deformation of the inversion base is clearly observable on Fig. 5.15 for the plume on the right (The isotemperature surface represented does not correspond rigorously to the inversion layer but will likely exhibit the same behavior as neighboring isotemperature surface are roughly parallel to each others). The air engulfed in the inversion layer by entrainment is colder than the one in the inversion thereby resulting in a negative heat flux at the inversion layer as noted previously (Fig. 5.4).

Another view of the flow is provided by Fig. 5.16. Following Schmidt & Schumann , the instantaneous dimensionless temperature fluctuations θ'/θ_C^6 (left) and vertical velocity (right) fields were plotted at dimensionless time $t_* = 6$ for differnet dimensionless heights: $z/z_i^6 = 0.05,\ 0.35,\ 0.65$ and 1.00 respectively.

In the bottom of the domain ($z/z_i^6 < 0.3$) we can distinctly spot the *spoke pattern* first discovered by Busse [43]. The spoke pattern consists of coherent structures formed by irregular polygons whose size typically varies around 1 to 2 z_i^6 (ie: 1-3 [km]). The updrafts are mostly limited to the thin walls of those polygonal and especially to the hub (ie: intersection of the walls). As illustrated by Fig. 5.16 vertical velocity is strongly correlated to the temperature variations in the lower layer of the CBL. As the plumes ascend, the spoke pattern attenuates. Plumes converge toward one of the main hubs or progressively decay under the influence of the large downdrafts. At $z/z_i^6 = 0.65$, the spoke pattern is not visible anymore, only the strongest plumes persist. They are clearly visible on the temperature fluctuations graph as zone of intense Fluctuations and are associated to upward velocity. Finally, two bottom contour plot provide us with another representation of the dome-lie structure observed in the CBL. Spots of cold rising are entrained in the inversion layer thereby pushing hot air down (ie: the blue ring on the vertical velocity plot) in the mixed layer.

5.4 Conclusion and perspectives

In this Chapter we tested and validated the code developed in the context of this thesis. In particular, we demonstrated that the results obtained were overall similar to the ones reported by Schmidt & Schumann. The three dimensional structure of the CBL was further investigated and compared to the descriptions found in the literature. Consistent correspondence between the structures described in the literature and the patterns observed in the simulations performed using BigFlow was established, thereby further validating our implementation. Nonetheless, a few elements need to retain our attention. First of all, we noticed that, although the rising rate of the inversion base computed matched the expression provided by Schmidt & Schumann, the starting height was not identical in both cases. Moreover, evidence of non uniform horizontal behavior of the horizontal velocity components was also found. To end with, we also put to question the need for a specific treatment of the upper boundary condition for the specific setup studied.

Beside investigating these unexpected behaviors, a interesting continuation to this thesis, could have been to extend to code to more complex cases. LES simulations in the context of ABL flows have become at the center of an increasing number of publications. The list of topics

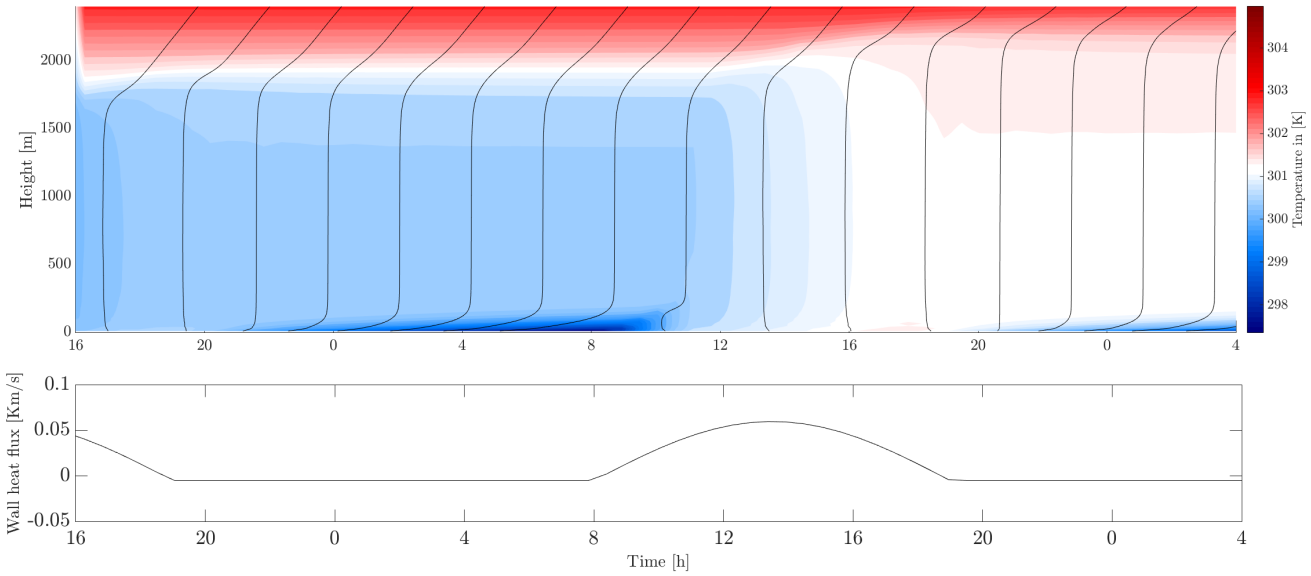

Figure 5.17: Simulation of a daily cycle. **Top plot:** Vertical variations of color indicate a change of the mean temperature of the flow with height. Evolution of the temperature profile over the course of one day and a half and temperature indicated in [K]. Vertical black profile represent the evolution of the horizontally averaged temperature profiles with time **Bottom plot:** Evolution of the wall kinematic heat flux expressed in [Km/s] as a function of the time expressed in [h]. Temperature profile based on Kumar [44]

to experiment with is basically endless. As a proof of concept, we tried to extend our code to the simulation of a diurnal cycle of the CBL. The simulation was run with the quasi steady solution of Schmidt & Schumann as an initial condition. The later corresponds to the state of the CBL in the mid-afternoon. A variable heat flux based on Kumar [44] was then applied at the wall resulting in variation of the flow's structure. The grid used had to be kept relatively coarse in order to keep the computational cost affordable. As illustrated on Fig. 5.17, this simplified setups already captures some of the distinctive features of the diurnal cycle described in Section 2.2. For example, the stable nocturnal resulting from the ground radiative cooling effect is clearly visible from around from 20:00 to 9:00.

Chapter 6

Conclusion

As a result of this thesis, significant improvements have been implemented in the BigFlow Navier-Stockes numerical solver to enhance the treatment of scalar fields in the context of Large Eddy Simulations (LES). These modifications were implemented with the ambition to model dry convective boundary layers (CBL). The new set of boundary conditions and discretization schemes developed had in term to provide us with a framework allowing to accurately model the turbulent structures present in dry convective boundary layers. A specific focus was nonetheless kept on implementing schemes and boundary conditions that were kept as general as possible thereby allowing to model other scalar fields such as the humidity field.

A first step consisted in extending the Subgrid Scale (SGS) modeling capabilities of BigFlow to scalar fields. This was achieved assuming the SGS Prandtl could be considered as constant and that the SGS scalar diffusivities were therefore taken directly proportional to the SGS viscosity. This approach, though simple, still implied the differentiation procedure had to be adapted to account for variable diffusivities.

The main achievement of this work was to design a new type of boundary condition that allows to prescribe scalar fluxes boundary conditions in the BigFlow wall modeling context. The problem we initially encountered was that, when wall models are used, inconsistent data was fetched into the ghost points beyond the walls which made the computation of the scalar convective term impossible. We thus developed and implemented an extension of the wall modeled boundary conditions first introduced by Thiry [17]. The resulting scalar boundary condition relied on the formulation of a modified version of the formulation of the differentiation schemes, the so called `DIVQ` version of the scalar discretization scheme, and on the implementation of an adaptive wall differentiation stencil in order to be used. The new version of the scalar scheme along with the new scalar flux boundary condition were then tested and validated against standard heated channel flow benchmark solution.

The implementation of the SGS model and scalar flux boundary conditions is not specific to the ABL, this problem can be met in many other fields. In addition to them, some more CBL specific considerations also had to be made. In practice, the atmosphere is not really bounded. Yet modeling the CBL require the use of a finite size domain which can truncate the physics of the problem. A Rayleight friction absorbing layer was developed to prevent spurious reflexions of gravity waves against the top of the domain thereby removing the non-physical influence from the upper rigid lid.

The final step was obviously to effectively apply the newly designed tools to ABL modeling. Validation was performed in the CBL flow context. CBLs offer a convenient framework for Atmospheric Boundary Layers LES validation as their study is widely documented in literature. The results obtained by Schmidt & Schumann were taken as a reference to validate our implementation. Schmidt & Schumann simulation corresponds to a CBL uniformly heated from below

and topped by a layer of uniformly stratified fluid under zero mean flow. Under these conditions, the flow is buoyancy driven and inherently linked to turbulent motions. Overall good match between the results computed by BigFlow and the ones of Schmidt & Schumann was observed. Even so, some strange behavior of the code were noticed. The two main one are respectively the anisotropic behavior of the horizontal velocity component and the difference in the height of the inversion predicted. Moreover the question of the usefulness of the absorbing layer in this context was raised. The three dimensional structure of the flow was also examined with good match between our results and the pattern predicted in the literature.

Our results were thus overall demonstrated good agreement with what we expected. Yet we barely scratched the surface of the ABL modeling complexity. ABL are inherently complex. Their formation results from intricated processes and complex force balances. Many possibilities could be envisioned regarding the continuation of this thesis as evidenced by the ever increasing number of publications on the subject. However, dependless on the application considered: whether it studies their temporal evolution, the effect of complex surface geometries, or the modeling of the humidity field, the implementation of a working of the comparatively *simple* dry CBL will always remain the required first step in that direction.

Bibliography

[1] J. R. Garratt. *The atmospheric boundary layer.* Cambridge University Press Cambridge ; New York, 1992.

[2] Roland B. Stull. *An introduction to boundary layer meteorology.* Springer, 1988.

[3] Denise Hertwig. *On Aspects of Large-Eddy Simulation Validation for Near-Surface Atmospheric Flows.* PhD thesis, Universität Hamburg, 2013.

[4] Giulia Ercolani. *Large-Eddy Simulation: A tool to study land-atmosphere interactions.* PhD thesis, Politecnico di Milano, 2014.

[5] M.W. Rotach and P. Calanca. Boundary layer (atmospheric) and air pollution: Microclimate. In Gerald R. North, John Pyle, and Fuqing Zhang, editors, *Encyclopedia of Atmospheric Sciences (Second Edition)*, pages 258 – 264. Academic Press, Oxford, second edition edition, 2015.

[6] Stefan Emeis. *Surface-Based Remote Sensing of the Atmospheric Boundary Layer*, volume 40. Springer Netherlands, 2011.

[7] A. S. Monin and A. M. Obukhov. Basic laws of turbulent mixing in the atmosphere near the ground. Technical Report 151, 1963-1987, SSSR Geophiz. Inst., Tr. Akad. Nauk., 1954.

[8] J. C. Kaimal and J. J. Finnigan. *Atmospheric Boundary Layer Flows: Their Structure and Measurement.* Oxford University Press Cambridge, 1992.

[9] Helmut Schmidt and Ulrich Schumann. Coherent structure of the convective boundary layer derived from large-eddy simulations. *Journal of Fluid Mechanics*, 200:511–562, 1989.

[10] J. Smagorinsky. General circulation experiments with the primitive equations. *Monthly Weather Review*, 91(3):99–164, 1963.

[11] Dries Allaerts. *Large eddy simulation of a large wind-turbine array in a conventionally neutral atmospheric boundary layer.* PhD thesis, KU Leuven, 2016.

[12] J. W. M. Cuijpers and P. G. Duynkerke. Large eddy simulation of trade wind cumulus clouds. *Journal of the Atmospheric Sciences*, 50(23):3894–3908, 1993.

[13] Shengbai Xie. *A numerical study of wind turbine wakes under various athmospheric stability conditions.* PhD thesis, University of Delaware, 2016.

[14] Laurent Georges. *Development and validation of a LES methodology for complex wall-bounded flows. Application to high order structured and industrial unstructured solvers.* PhD thesis, Université catholique de Louvain, 2007.

[15] Laurent Bricteux. *Simulation of turbulent aircraft wake vortex flows and their impact on the signals returned by a coherent Doppler LIDAR system.* PhD thesis, Université catholique de Louvain, 2008.

[16] Matthieu Duponcheel. *Direct and large-eddy simulation of turbulent wall-bounded flows: further development of a parallel solver, improvement of multiscale subgrid models and investigation of vortex pairs in ground effect.* PhD thesis, Université catholique de Louvain, 2009.

[17] Olivier Thiry. *Investigation of wall shear stress models for large eddy simulation.* PhD thesis, Université catholique de Louvain, 2016.

[18] Oleg V. Vasilyev. High order finite difference schemes on non-uniform meshes with good conservation properties. *Journal of Computational Physics*, 157(2):746 – 761, 2000.

[19] Francis H. Harlow and J. Eddie Welch. Numerical calculation of time-dependent viscous incompressible flow of fluid with free surface. *The Physics of Fluids*, 8(12):2182–2189, 1965.

[20] D. K. Lilly. The representation of small scale turbulence in numerical simulation experiments. pages 195–210, 1967.

[21] Cedric Dall'Ozzo. *Modélisation d'écoulements atmosphériques stratifiés par Large-Eddy Simulation à l'aide de Code_Saturne.* PhD thesis, Université Paris-Est, 2013.

[22] Andreas Bechmann. *Large-Eddy Simulation of Atmospheric Flow over Complex Terrain.* PhD thesis, Technical University of Denmark, 2006.

[23] Marcelo Chamecki Diana M. Cancelli and Nelson L. Dias. A large-eddy simulation study of scalar dissimilarity in the convective atmospheric boundary layer. *Journal of the Atmospheric Sciences*, 71(1):3–15, 2014.

[24] Kleissl Jan, Kumar Vijayant, Meneveau Charles, and Parlange Marc B. Numerical study of dynamic smogorinsky models in large-eddy simulation of the atmospheric boundary layer: validation in the stable and unstable case. *Water Resources Research*, 42(6), 2006.

[25] Stoll Rob and Porté-Agel Fernando. Dynamic subgrid-scale models for momentum and scalars fluxes in large eddy simulations of neutrally stratified atmosphric boundary layers over heterogenous terrain. *Water Resources Research*, 42(1), 2006.

[26] Qi Li, Elie Bou-Zeid, William Anderson, Sue Grimmond, and Marcus Hultmark. Quality and reliability of les of convective scalar transfer at high reynolds numbers. *International Journal of Heat and Mass Transfer*, 102:959 – 970, 2016.

[27] T.H. Shih and N. N. Mansour. Modeling of near-wall turbulence. Technical report, NASA, Cleveland, Ohio, 1990.

[28] U. Schumann. Subgrid scale model for finite difference simulations of turbulent flows in plane channels and annuli. *Journal of Computational Physics*, 18(4):376 – 404, 1975.

[29] Hiroshi Kawamura, Kouichi Ohsaka, Hiroyuki Abe, and Kiyoshi Yamamoto. Dns of turbulent heat transfer in channel flow with low to medium-high prandtl number fluid. *International Journal of Heat and Fluid Flow*, 19(5):482 – 491, 1998.

[30] M. Duponcheel L. Bricteux and G. Winckelmans. A multiscale subgrid model for both free vortex flows and wall-bounded flows. *Physics of Fluids*, 21(10):105102, 2009.

[31] Qiang Li, Philipp Schlatter, Luca Brandt, and Dan S. Henningson. Direct numerical simulation of a turbulent boundary layer with passive scalar transport. In Vincenzo Armenio, Bernard Geurts, and Jochen Fröhlich, editors, *Direct and Large-Eddy Simulation VII*, pages 321–327, Dordrecht, 2010. Springer Netherlands.

[32] Joseph B. Klemp and Dale R. Durran. An upper boundary condition permitting internal gravity wave radiation in numerical mesoscale models. *Monthly Weather Review*, 111(3):430–444, 1983.

[33] Urska Bajec. Boundary conditions for nested limited area meteorological models, October 2010.

[34] Paolo Davini, Fabio D'Andrea, Seung-Bu Park, and Pierre Gentine. Coherent structures in large-eddy simulations of a nonprecipitating stratocumulus-topped boundary layer. *Journal of the Atmospheric Sciences*, 74(12):4117–4137, 2017.

[35] Chiel C. van Heerwaarden, Juan Pedro Mellado, and Alberto De Lozar. Scaling laws for the heterogeneously heated free convective boundary layer. *Journal of the Atmospheric Sciences*, 71(11):3975–4000, 2014.

[36] Robert J. Conzemius and Evgeni Fedorovich. Large eddy simulation of realistic wind fields in daytime atmospheric boundary layer, May 2010.

[37] James W. Deardorff. Convective velocity and temperature scales for the unstable planetary boundary layer and for rayleigh convection. *Journal of the Atmospheric Sciences*, 27(8):1211–1213, 1970.

[38] J. W. Deardorff and G. E. Willis. Further results from a laboratory model of the convective planetary boundary layer. *Boundary-Layer Meteorology*, 32(3):205–236, Jul 1985.

[39] G. E. Willis and J. W. Deardorff. A laboratory model of the unstable planetary boundary layer. *Journal of the Atmospheric Sciences*, 31(5):1297–1307, 1974.

[40] Charles Meneveau and Joseph Katz. Scale-invariance and turbulence models for large-eddy simulation. *Annual Review of Fluid Mechanics*, 32(1):1–32, 2000.

[41] J. B. Klemp and D. K. Lilly. Numerical simulation of hydrostatic mountain waves. *Journal of the Atmospheric Sciences*, 35(1):78–107, 1978.

[42] James Sandham and Michael L. Waite. Spectral energy balance in dry convective boundary layers. *Journal of Turbulence*, 16(7):650–675, 2015.

[43] F. H. Busse and J. A. Whitehead. Oscillatory and collective instabilities in large prandtl number convection. *Journal of Fluid Mechanics*, 66(1):67–79, 1974.

[44] Vijayant Kumar, Gunilla Svensson, A. A. M. Holtslag, Charles Meneveau, and Marc B. Parlange. Impact of surface flux formulations and geostrophic forcing on large-eddy simulations of diurnal atmospheric boundary layer flow. *Journal of Applied Meteorology and Climatology*, 49(7):1496–1516, 2010.

Rue Archimède, 1 bte L6.11.01, 1348 Louvain-la-Neuve **www.uclouvain.be/epl**